BUBBLE FORMATION DURING HORIZONTAL GAS INJECTION INTO DOWNWARD FLOWING LIQUID

Hua Bai and Brian G. Thomas

Hua Bai, Senior research engineer, is with the Dow Chemical Company, 2301 N. Brazosport Blvd., Freeport, TX 77541, and Brian G. Thomas, Professor, are with the Department of Mechanical and Industrial Engineering, University of Illinois at Urbana-Champaign, 1206 West Green Street, Urbana, IL 61801

ABSTRACT

Bubble formation during gas injection into turbulent downward flowing water is studied using high-speed videos and mathematical models. Bubble size is determined during the initial stages of injection and is very important to turbulent multiphase flow in molten metal processes. The effects of liquid velocity, gas injection flow rate, injection hole diameter, and gas composition on initial bubble formation behavior have been investigated. Specifically, bubble shape evolution, contact angles, size, size range and formation mode are measured. Bubble size is found to increase with increasing gas injection flow rate and decreasing liquid velocity, and is relatively independent of gas injection hole size and gas composition. Bubble formation occurs in one of four different modes, depending on liquid velocity and gas flow rate. Uniform-sized spherical bubbles form and detach from the gas injection hole in Mode I for low liquid speed and small gas flow rate. Modes III and IV occur for high velocity liquid flows where the injected gas

elongates down along the wall and breaks up into uneven sized bubbles. An analytical two-stage model is developed to predict the average bubble size, based on realistic force balances, and shows good agreement with measurements. Preliminary results of numerical simulations of bubble formation using a VOF model qualitatively match experimental observations, but more work is needed to reach a quantitative match. The analytical model is then used to estimate the size of the argon bubbles expected in liquid steel in tundish nozzles for conditions typical of continuous casting with a slide gate. The average argon bubble sizes generated in liquid steel are predicted to be larger than air bubbles in water for the same flow conditions. However, the differences lessen with increasing liquid velocity.

KEY WORDS: Bubble formation, Turbulent flow, Steel continuous casting, Argon gas injection, Slide-gate nozzle

I. INTRODUCTION

Gas is injected into flowing liquid during many important processes. Bubbles form during the initial stages of gas injection, which govern their shape and size distribution. Bubble size is very important to subsequent turbulent flow phenomena for several reasons. In the processing of molten metals, argon gas is often injected to encourage liquid stirring, to help remove inclusions, and to help prevent reoxidation and clogging.

In the continuous casting of steel, for example, argon gas is injected horizontally through tiny holes on the inner wall of the nozzle, which connects the tundish and mold.

The injected gas encounters liquid steel flowing downward across its path. The downward liquid flow exerts a strong shear force on the forming bubble, which greatly affects its formation. If the gas stretches into a long sheet along the wall, the flow will behave very differently than if the gas stream simply breaks up into small bubbles that mix quickly with the liquid.

Knowing the bubble size is essential for studies of multiphase flow and related phenomena. The flow pattern in the continuous casting mold has been shown to depend on both the injection rate and the size of argon bubbles [1-3]. Furthermore, small bubbles can penetrate deep into the liquid pool and become entrapped by the solidified shell, causing quality problems, such as "pencil pipe" blister defects [4, 5]. Wang et al. [6] reported that an optimal bubble size exists for inclusion removal. Tabata et al. [7] performed water model tests to study the gas injection into the slide-gate nozzle, and found that large bubbles tended to move to the center of flow, thus lowering their ability to catch inclusions and to prevent their adherence to the nozzle wall.

This work was undertaken to increase understanding of the initial stages of bubble formation during horizontal gas injection into downward flowing liquid. Specifically, this work aims to quantify the bubble size as a function of important process parameters by first measuring air bubble size from injection into flowing water. Next, mathematical models are developed to accurately predict the bubble size measurements. Finally, the best model is applied to estimate the size of bubbles expected during argon injection into flowing steel under conditions typically encountered in tundish nozzles used in the continuous casting of steel.

II. PREVIOUS WORK

Previous work on bubble formation in liquid metals includes a few experimental studies on gas-stirred vessels with gas injected from an upward-facing orifices or tubes submerged in relatively quiescent liquid. The frequency of bubble formation was measured by using pressure pulse [8, 9], resistance probe [10, 11], or acoustic devices [12]. The mean bubble volume and the corresponding equivalent diameter are then derived from the known gas injection flow rate and the frequency of bubble formation. Efforts to directly observe bubble formation in liquid metal have been made using X-ray cinematography [13, 14].

No theoretical modeling studies have been reported for bubble formation in metallic systems. However, extensive studies of bubble formation have been done on aqueous systems, both experimentally and theoretically, as reviewed by Kumar and Kuloor [15], Clift et al. [16], Tsuge [17], and Rabiger and Vogelpohl [18]. Recently, Wang et al [19] used water models to study air bubble formation from gas injected through porous refractory into an acrylic tube with flowing water. Wettability was reduced by waxing the nozzle walls, which caused the bubbles to coalesce together, form a gas curtain traveling along the wall, and then break into many uneven-sized bubbles. On an unwaxed surface, uniform-sized bubbles formed and detached from the wall to join the liquid flow.

Most previous studies modeled bubble formation in stagnant liquid. The theoretical studies fall into two categories: analytical models of spherical bubbles and discretized models of non-spherical bubbles. The spherical bubble models solve a force balance equation and/or bubble motion equation for the size of the growing spherical bubble at detachment. Forces are evaluated for the entire growing bubble. Two of many

significant contributions are the single-stage model of Davidson and Schuler [20] and the two-stage model of Kumar and Kuloor [21]. These models adopt empirical criteria to determine the instant of detachment.

In contrast, non-spherical bubble models have been developed [22-25] that are based on a local balance of pressure and force at the gas/liquid interface. In these models, the bubble surface is divided into many two-dimensional axisymmetric elements. For each element, equations of motion in both the radial direction and vertical directions are solved for the radial and vertical velocities, which are used to find the position of each element. The bubble growth and bubble detachment is determined by calculating the (non-spherical) shape of the bubble during its formation. These models have the advantage that empirical detachment criteria are not required. Unfortunately, they are not applicable to non-axisymmetric conditions such as arise with shearing flowing liquid. Even full numerical simulation of bubble formation was reported by Hong et al., [26] who modeled the formation of a bubble chain in stagnant liquid by tracking the movement of the discretized gas-liquid interface using the VOF (Volume of Fluid) method in CFD. [27]

Only a few studies [28-30] have modeled bubble formation with flowing liquid. In these models, the analytical models of spherical bubble formation in stagnant liquid are modified to accommodate uniform liquid flow by adding a drag force due to the flowing liquid in the equation of motion. More empirical parameters are introduced in order to match experimental results, so these models are limited to the particular systems and conditions of the measurements.

III. WATER MODEL EXPERIMENTS

Water model experiments are performed to investigate bubble formation during gas injection through tiny horizontal pores into turbulent liquid flowing vertically down the wall. This shears the growing bubbles from the wall under flow conditions that incorporate the essential phenomena in tundish nozzle flow. High-speed video photography is used to visualize the effects of liquid velocity, gas injection flow rate, gas injection hole size, and gas composition on the bubble size, shape, frequency, mode, and size distribution. In addition to quantifying these important parameters, the results of these water experiments also serve to validate the theoretical model developed later.

A. Experimental apparatus and procedure

Figure 1 shows a schematic of the experimental apparatus. Water flows down from an upper tank that simulates a tundish, through a vertical tube that simulates a tundish nozzle, and into a tank at the bottom that simulates a casting mold. The gas (air, helium, or argon) is injected through a plastic tube attached to a hollow needle inserted horizontally into a square 35mm X 35mm Plexiglas tube. Water is made to flow downward for conditions approximating those in a tundish nozzle. The needle outlet is aligned flush with the nozzle wall to simulate a pierced hole on the inner wall of a nozzle. Three different-sized needle hole sizes are used to examine the effect of the gas injection hole diameter (0.2, 0.3, and 0.4 mm). The gas flow controller is adjusted to achieve volumetric gas flow rates of 0.17 - 6.0ml/s per orifice. Water flow rate is adjusted by partially blocking the bottom of the nozzle. The average water velocity varies from 0.6m/s to 3.1m/s, which corresponds to pipe Reynolds numbers of 21,000 - 109,000. The

water velocity is obtained by measuring from the video frames, the average speed of tracer particles which are added to the water.

The formation of bubbles is recorded by a video camera at 4500 frames per second. Each recorded sequence contains 1000 frame images taken over 0.22 second. This high speed was necessary to capture the rapid events that occur during bubble formation. The vertical head of liquid, from the top surface of the liquid in the upper tank to the needle, is about 500mm and drops less than 20mm during video recording, owing to the short measurement time. The behavior of bubbles exiting from the needle hole is studied by inspecting the sequences of video images frame by frame. The frequency (f) of bubble formation is determined by counting the number of the bubbles generated at the exit of the injection hole during the recorded time period. The mean bubble volume (V) is then easily converted from the known gas injection volumetric flow rate (Q_g), via

$$V = \frac{Q_g}{f} \tag{1}$$

An equivalent average bubble diameter (D) is calculated assuming a spherical bubble, or

$$D = \left(\frac{6Q_g}{\pi f} \right)^{1/3} \tag{2}$$

Bubbles sizes are also measured directly from individual video images in order to validate this procedure and to check the bubble size deviation from its average value. In some tests, a second needle is inserted into the nozzle wall 12.5mm downstream below the first needle in order to study the interaction between bubbles from adjacent gas injection sites.

B. Bubble size in stagnant liquid

Experiments are first performed with stagnant water where previous measurements and models are available for comparison. This was accomplished simply by keeping the bottom of the tube closed. Although most previous studies are based on bubble formation from an upward facing orifice or nozzle, some authors [12, 15] observed that bubbles formed from a horizontal orifice behaved almost the same in stagnant liquid. Figure 2 shows the measured bubble diameters together with a prediction using Iguchi's empirical correlation [14]. Iguchi's equation is a curve fit of bubble sizes measured at relatively large gas flow rates injected vertically into stagnant liquid. The agreement is reasonably good, which confirms that this equation also applies to horizontal injection at the relatively low gas flow rates of this work.

The results in Figure 2 show that bubble size increases with increasing gas injection flow rate. For the same gas injection rate, a bigger injection orifice produces larger bubbles. At high gas injection rates, larger bubbles emerge from larger diameter orifices. However, orifice size becomes less important at small gas injection rates.

C. Bubble size in flowing liquid

Experiments are next performed with gas injected into flowing water. The measured mean bubble sizes are plotted in Figure 3. Each point in Figure 3 represents the mean bubble diameter obtained from the measured frequency using Equations 1 and 2 for a single test with a particular gas injection flow rate, water velocity and gas injection hole size. In addition, the maximum and minimum bubble sizes were obtained by directly measuring the video images for each test. This range of bubble sizes is shown as "error

bars" for each point. Also shown on the figure is the symbol (circle, triangle or square) representing the corresponding bubble formation mode that is discussed in section D.

Figure 3 shows that the mean bubble size increases with increasing gas flow rate and decreasing water velocity. Comparing Figures 2 and 3, it can be seen that at the same gas injection flow rate, the bubble size in flowing liquid is much smaller than in stagnant liquid. This becomes much clearer when the volumes of bubbles formed in stagnant and flowing liquid are plotted together, as shown in Figure 4. The bubble volumes formed in flowing water are 5 to 8 times smaller than those in stagnant water.

Physically, the smaller bubble size in flowing liquid is natural because the drag force from the liquid flow along the wall acts to shear the bubbles away from the tip of the gas injection hole into the liquid stream before they have time to grow to the mature sizes found in stagnant liquid. Moreover, Figure 3 also shows clearly that for a given gas flow rate, the higher the velocity of the shearing liquid flow, the smaller are the detached bubble sizes.

The combined effects of gas injection rate, liquid velocity and gas composition on bubble volume are shown together in Figure 5. The trends are identical to those in Figure 3, except that the differences in bubble volume are magnified relative to those in diameter. All of the experimental data shown in Figures 2-4 are for air. Further experiments with argon and helium investigated the effect of gas compositions. Figure 5 shows that the measured mean bubble sizes for three different gases (air, argon and helium) are all about the same. Thus, the gas composition has little influence on bubble size.

It appears that bubble size is relatively independent of gas injection hole size. This can be seen by comparing Figures 3(a), (b) and (c). This observation is different from that in stagnant liquid, where bubble size is slightly larger for larger injection hole. This suggests that the shearing force due to the flowing liquid dominates over other effects related to the hole size such as the surface tension force.

Figures 2-5 show that the data collected with higher water velocities generally also tend to have higher gas flows. This choice of test conditions was an unplanned consequence of the greater water flow inducing lower pressure at the orifice, which consequently increased gas flow rate. The higher-speed flowing liquid acts to aspirate more gas into the nozzle. This observation illustrates the important relationship between liquid pressure and gas flow rate that should be considered when investigating real systems.

D. Bubble formation mode

The initial shape of the bubble growing and exiting the gas injection hole was observed to behave in one of four distinct modes, shown in the representative recorded images of Figure 6. Figure 7 shows sequences of recorded images for two tests which illustrate two of these modes. The detailed stages of bubble formation are illustrated more clearly by tracing these images, as shown in Figure 8.

Figure 6 shows close-up photos of bubbles exiting pairs of injection holes for each mode. The upper four frames show side views, including the nozzle wall (right). This view is complicated by the dark portion of the nozzle wall where the needle is inserted, and by the edges of plastic supports, which are both outside of the model and have no influence on the flow. The lower frames in Figure 6 show the perpendicular end

views for three modes, looking at the nozzle wall into the injection hole (all same scale). Schematic tracings of two dark photos are included for clarity.

For low velocity water flows (less than 1m/s) and small gas injection rates (less than 2ml/s), Mode I is observed. In this mode, uniform-sized spherical bubbles form at the tip of the gas injection hole, as shown in Figures 6 (a), (e) and (f). Each bubble elongates slightly before it discretely detaches from the hole and joins the liquid stream, as a spherical bubble again. This sequence of events is shown in ten steps in Figures 7(a) and 8(a). The entire process needs only 0.004s for these conditions. For this mode, no interaction was observed between bubbles flowing from the upper injection hole and those from the lower hole, when it was there. It is expected that such independent behavior of the bubbles would be observed even for gas flow through porous refractories, where the individual pores which actively emit bubbles might be spaced closer together. Thus, mode I corresponds to bubbly flow.

At the other extreme, Mode IV is observed for high velocity water flows (more than 1.6m/s) and very large gas injection rates (more than 10ml/s). In this mode, each bubble elongates down along the wall and forms a sheet or curtain. This curtain merges with the gas from the lower hole, if it exists, to form a long, wide continuous gas curtain. Both the thickness and width of the curtain increase with distance below the injection hole, as shown in Figures 6 (d) and (i). This is due to the gradual decrease in downward gas velocity, as the buoyancy forces increase. This mode likely leads to the detrimental "annular" flow condition, where the gas and liquid phases separate into large fluctuating regions [31]. The curtain eventually becomes unstable when its thickness becomes too great and it breaks up into many bubbles with different sizes. Their sizes range from a few that

are very large to others that are very tiny. For the range of gas flow rates of practical interest to gas injection into steel nozzles, this regime is not expected.

Mode III is observed for conditions of high water velocity (more than 1.6m/s) and for gas injection flow rates typical of steel casting (less than 6ml/s). Mode III is similar to Mode IV except that there is insufficient gas flow to maintain a continuous gas curtain, so gaps form. Before detaching from the gas injection hole, Figures 7(b) and 8 (b) document how the bubbles in this mode simultaneously expand and elongate to reach almost twice their diameter by the instant of detachment. The bubbles continue to elongate as they move down along the wall. They remain against the wall for some distance below the injection hole before moving off to join the general flow. When a second (lower) injection hole exists, the two bubble streams often coalesce to form larger elongated bubbles. This further contributes to the non-uniform size distribution. Figures 6 (c), (g) and (h) show the ellipsoidal shape of bubbles resulting from this mode.

Mode II is a transitional mode between Modes I and III in which the injected gas initially elongates along the wall but quickly detaches from it. When two gas injection holes are used, the bubbles from the upper hole do not coalesce with bubbles from the lower hole for cases classified as Mode II. Bubbles sizes for Mode II are still relatively uniform compared to those in Modes III and IV.

E. Mode and size range

In addition to the measured mean bubble size, Figure 3 also shows the mode and the bubble size range, represented by error bars. Higher liquid velocities keep the bubbles closer to the wall. Higher gas flows tend to make the gas stream continuous. All cases with water velocity of 0.9m/s or less fall into Mode I and have a very tight size

distribution, which corresponds to relatively uniform spherical bubbles detaching near the tip of the hole. Most of the cases in Figure 3 with a water velocity about 1.4m/s fall into Mode II and have slightly wider size ranges. All cases with liquid velocity of 1.9m/s or more fall into either Mode III or Mode IV, and have huge size ranges, which corresponds to the break-up of a discontinuous gas curtain into uneven-sized bubbles. Bubble diameters as small as 0.5mm are measured. The continuous gas curtain in Mode IV is observed only at very high gas flow rates, (Q_g > 10 ml/s per hole), which is beyond the practical range of interest, so is not shown in the plots.

F. Bubble elongation measurement

The bubble is observed to grow and elongate during its formation. To quantify the bubble shape during this process, the vertical elongation length of the bubble (L) is measured at the instant of detachment of the bubble from its injection hole, as shown in Figure 9(a). The measured bubble elongation lengths are plotted for different gas flow rates and liquid velocities in Figure 9(b). The effects become more clear when plotting the elongation factor, e_d, defined as the ratio of the elongation length (L) and the equivalent bubble diameter (D_d) (defined using Equations 1 and 2 which assume a spherical bubble with the same volume)

$$e_d = \frac{L}{D_d} \tag{3}$$

As shown in Figure 10(a), the elongation factor varies from 1.3 to 1.8 and depends mainly on the liquid velocity. It is relatively independent of the gas injection flow rate. Bubbles elongate slightly more at higher liquid velocity. Figure 10(b) illustrates this

effect of liquid velocity, U, on the measured average elongation factors. These four data points are well fitted with a simple quadratic function,

$$e_d = 0.78592 + 0.70797U(m/s) - 0.12793U(m/s)^2 \quad (4)$$

G. Contact angle measurement

Contact angles were measured from the bubble photographs in this work in order to better evaluate the surface tension forces acting on the bubble. The surface tension forces depend on the contact angles between the bubble and the wall as follows [32],

$$F_{Sz} = \frac{\pi}{2} r \sigma f_\theta \quad (5)$$

where the contact angle function, f_θ, depends on the static contact angle, θ_0, and the difference between the contact angles above and below the bubble,

$$f_\theta = \sin\theta_o \left(\cos\theta_r - \cos\theta_a\right) \quad (6)$$

The static contact angle is defined by the profile adopted by a liquid drop at rest on a flat horizontal surface and was measured to be 50° for the current water / air / solid-plastic system. The flowing liquid alters the contact angle around the interface circumference, as shown in Figure 11(a). Stretching of the upstream edge of the bubble increases the contact angle, defined there as the advancing contact angle, θ_a. Compressing of the downstream edge of the bubble decreases the contact angle, defined there as the receding contact angle, θ_r.

Table I shows the mean contact angles measured in the water experiments. With increasing liquid velocity, the advancing contact angle θ_a increases, and the receding contact angle θ_r decreases. The effect of gas flow rate is relatively small. The contact

angle function f_θ increases with increasing liquid velocity, as plotted in Figure 12. The four data points are well fitted with a simple quadratic function,

$$f_\theta(U) = -0.06079 + 0.33109U(m/s) + 0.078773U(m/s)^2 \qquad (7)$$

IV. ANALYTICAL MODEL FOR BUBBLE SIZE PREDICTION

The formation of bubbles during horizontal gas injection into vertical fast-flowing liquid is very different from the classic bubble formation problem of vertical gas injection into stagnant liquid, studied with many previous models. When horizontally-injected gas encounters severe downward shearing forces, smaller bubbles result, as documented by the measurements in the previous section. Unlike bubble formation in stagnant liquid, in which buoyancy is the major driving force for bubble detachment, the buoyancy force here acts to resist bubble detachment against the drag force of downward liquid momentum. Thus, a new analytical model had to be developed, based on balancing the forces acting on the growing bubble and setting a proper bubble detachment criterion.

A. Forces acting on a growing bubble

Correct evaluation of the fundamental forces acting on the growing bubble is essential for an accurate analytical model of bubble formation that can be extrapolated to other systems. A schematic of the fundamental forces acting on a growing bubble is shown in Figure 13. The forces of liquid drag, buoyancy, and surface tension are now discussed in turn.

Drag force due to flowing liquid F_D

The liquid flowing down the wall exerts a downward drag force on the growing bubble, F_D, which depends on the exact nature of the steep liquid velocity profile near the wall. A reasonable and convenient equation describing the velocity profile for fully developed turbulent flow in a pipe, is the seventh root law profile [33]

$$u = 1.235U\left(\frac{y}{D_N / 2}\right)^{1/7} \tag{8}$$

where y is the distance from the wall, D_N is the nozzle diameter, and U is the mean vertical liquid velocity in the nozzle. The steady average liquid velocity across the growing bubble, $\bar{u}$, depends on the instantaneous bubble size and is estimated from

$$\bar{u} = \frac{1}{2r}\int_{y=0}^{y=2r} u dy = 1.3173U\frac{r^{1/7}}{D_N^{1/7}} \tag{9}$$

where r is the equivalent horizontal radius of the forming bubble. The drag force acting on the growing bubble, F_D, is

$$F_D = C_D\frac{1}{2}\rho_l\bar{u}^2\pi r^2 \tag{10}$$

Assuming the bubble Reynolds number, Re_{bub}, is less than 3×10^5, the drag coefficient C_D is [16]

$$C_D = \frac{24}{\mathrm{Re}_{bub}}(1+0.15\mathrm{Re}_{bub}{}^{0.687}) + 0.42/(1+4.25\times10^4\,\mathrm{Re}_{bub}^{-1.16}) \tag{11}$$

where Re_{bub} is defined by

$$Re_{bub} = \frac{\bar{u}D}{\upsilon} \tag{12}$$

where D is the equivalent bubble diameter and υ is the kinematic viscosity of the liquid. This downward drag force naturally increases as the bubble grows and extends into faster moving fluid.

Buoyancy force F_B

The upward buoyancy force of the low density gas acts to resist the drag force of the liquid momentum. This force increases simply and dramatically with increasing bubble diameter:

$$F_B = V_b(\rho_l - \rho_g)g = \frac{1}{6}\pi D^3(\rho_l - \rho_g)g \tag{13}$$

Surface tension force F_S

A surface tension force arises when the bubble deforms and its upper and lower contact angles differ, according to Equation 5 as discussed earlier. The vertical component of this force acts upward to resist the downward drag and keep the bubble attached to the gas injection hole. It increases as the bubble grows because of both the increasing bubble radius and the increasing deformation of the bubble as its shape elongates.

B. Two-stage model for bubble formation

The relative increases of the three fundamental forces acting on the bubble as it grows are compared in Figure 14, based on the equations just presented. Other forces, such as the inertial force due to the rate of change of momentum of the growing bubble, are believed to be negligible. A two-stage model is developed to predict the size of the bubbles formed by balancing these forces and then applying a reasonable detachment criterion. Bubble formation is assumed take place in two idealized stages, the expansion stage and the elongation stage, as shown in Figure 15.

Expansion stage

During the expansion stage, the bubble expands while holding onto the tip of the gas injection hole. This stage is assumed to end when the downward forces are first able to balance the upward force. That is,

$$F_D = F_B + F_{Sz} \tag{14}$$

The shape of the bubble during this stage is not considered until at the instant of the force balance when it is assumed to be spherical. Substituting Equations 5, 10 and 13 into Equation 14 yields

$$C_D \frac{1}{2}\rho_l \bar{u}^2 \pi r^2 = \frac{4}{3}\pi r^3(\rho_l - \rho_g)g + \frac{1}{2}\pi r\sigma \sin\theta_O(\cos\theta_r - \cos\theta_a) \tag{15}$$

In Equation 15, $\bar{u}$ depends on r, which is the unknown. Thus, Equations 9 and 15 are solved simultaneously for r by trial and error to yield r_e, which is the equivalent radius of the bubble at the end of the expansion stage.

Elongation stage

As the bubble continues to grow, the downward force eventually exceeds the upward forces acting on the bubble. This makes the growing bubble begin to move downward along with the liquid flow. The bubble keeps expanding since it still connects to the gas injection hole, and at the same time it elongates due to the shearing effect of the liquid flow.

During this elongation stage, the shape of the bubble is idealized as an ellipsoid. It is assumed to connect with the injection hole through a thin neck with negligible volume. The two horizontal radii of the ellipsoid, in the x and y directions, are assumed to be equal to r for simplicity.

The vertical radius of the ellipsoid (r_z) incorporates bubble elongation and is related to the equivalent bubble diameter (D) and the elongation factor (e) by

$$r_z = \frac{1}{2} eD \tag{16}$$

The volume of the ellipsoidal bubble is equated to an equivalent diameter spherical bubble (D),

$$\frac{4}{3}\pi\, r^2 r_z = \frac{1}{6}\pi D^3 \tag{17}$$

The instantaneous equivalent diameter (D) of the bubble is related to the instantaneous horizontal radius (r) of the ellipsoid and the instantaneous elongation factor (e) by rearranging Equations 16 and 17:

$$D = 2r\sqrt{e} \tag{18}$$

The bubble elongates more as it grows. The bottom of the ellipsoidal bubble is assumed to travel with the liquid at the average velocity $\bar{u}$, defined in Equation 9. The criterion to end this final stage of bubble growth is when the bubble elongates to the measured elongation at detachment from the gas injection hole, defined by e_d. This critical length of the bubble at the instant of detachment is related to the time needed for the fluid to travel from point A to B in Figure 15 (b).

$$\int_{t_e}^{t_d} \bar{u}\, dt = e_d D_b + \frac{d}{2} - r_e \tag{19}$$

where times t_e and t_d indicate the end of the expansion stage and the instant of bubble detachment respectively. r_d is the horizontal radius at detachment.

The time during bubble growth (t) is related to the instantaneous horizontal radius of the growing ellipsoidal bubble (r) by volume conservation, which assumes that pressure and temperature are sufficient uniform to avoid compressibility effects.

$$Q_g t = \frac{1}{6}\pi D^3 \tag{20}$$

Assuming that the bubble elongates linearly from 1 (spherical bubble at t_e) to e_d (detachment at t_d), the elongation factor evolves according to:

$$e = ar + b \qquad at \quad r_e \le r \le r_d \tag{21}$$

where the constants a and b are:

$$a = \frac{e_d - 1}{r_d - r_e} \tag{22}$$

$$b = \frac{r_d - e_d r_e}{r_d - r_e} \tag{23}$$

Inserting Equations 18 and 21 into Equation 20 and differentiating gives,

$$dt = d\left(\frac{4\pi}{3Q_g} r^3 e^{3/2}\right) = \frac{4\pi}{Q_g}\left(r^2 (ar+b)^{3/2} + \frac{ar^3}{2}(ar+b)^{1/2}\right)dr \tag{24}$$

Substituting Equations 9, 18 and 24 into Equation 19 yields the final model,

$$5.2692\frac{\pi U}{Q_g D_N^{1/7}} \int_{r_e}^{r_d} \left(r^{15/7}(ar+b)^{3/2} + \frac{ar^{22/7}}{2}(ar+b)^{1/2}\right)dr = 2r_d e_d^{3/2} + \frac{d}{2} - r_e \tag{25}$$

Equation 25 is solved for the horizontal radius of the ellipsoidal bubble at the instant of detachment from the gas injection hole, r_d, which is the only unknown in this equation, using trial and error iteration with a program written in MATLAB detailed elsewhere [34]. The equivalent bubble diameter at detachment is then found by inserting r_d and e_d into Equation 18.

It should be noted that there are no adjustable parameters in this model. The elongation factor at the instant of the bubble detachment (e_d) and the contact angle function (f_θ) depend on the mean liquid velocity (U), and are based directly on the experimental measurements, using empirical Equations 4 and 7 in the model.

V. COMPARISON OF MODEL PREDICTIONS AND MEASUREMENTS

The bubble diameters predicted by the two-stage model are shown in Figure 16, together with the measured mean bubble diameters. The fluid properties and operating conditions used in the calculation are given in Table II.

Figure 16 shows that the match between the model prediction and the experimental data is reasonably good, although the bubble diameter appears to be slightly over-predicted at low gas injection rates. This agreement is remarkable considering the crude assumptions regarding bubble shape and the lack of calibration parameters in the model.

The model and experiments show the same trends for the effects of the liquid velocity and gas flow rate. Specifically, the mean bubble size increases with increasing gas injection flow rate and decreasing liquid velocity.

The model predicts that the gas injection hole size has little effect on the bubble size at high liquid velocity ($U \geq 1.4$m/s). This is consistent with the water experiments, where it is difficult to distinguish between data measured from different hole sizes. However, at low liquid velocity, ($U \leq 0.9$m/s), the influence of the hole size increases, as shown in Figure 16 (a) and the larger gas injection hole generates slightly larger bubbles. This trend suggests a smooth transition from the behavior observed in stagnant liquid,

where gas injection hole size is very important, to the high liquid velocities in Figures 16(b)-(d).

The analytical model also predicts a negligible effect of the gas density that again matches the experimental measurements. The gas density only appears together with the liquid density in the $(\rho_l-\rho_g)$ term of Equation 15, where it is clearly negligible.

VI. NUMERICAL MODEL

The analytical two-stage model conveniently and accurately predicts the average bubble size in the system of interest in this study. It does not predict other important gas bubble behavior such as bubble formation mode, bubble shape, bubble size deviation, bubble coalescence and break-up, and the interaction between the bubbles and the liquid flow. Direct numerical simulation of bubble formation is a potential method to overcome this limitation.

The Volume of Fluid (VOF) method, developed by Nichols and Hirt [27] is well suited to model the flow of liquid coupled with the movement of a gas-liquid interface by solving local-instantaneous conservation equations and boundary conditions. This method employs an algorithm to track the free surface moving through a computational grid. Previous simulation of a single bubble chain in stagnant liquid using this VOF method has been reported [26] to agree well with the experimental results in a real time sequence. The method was applied here to simulate bubble formation during the horizontal injection of gas into vertical water flow measured in this work.

A. VOF Model Description

In this VOF method, differential conservation equations are solved only in the liquid phase. The gas-liquid interface, which forms the bubble surface, is treated as a movable pressure boundary. This boundary between the gas and liquid phases moves to maintain a prescribed constant pressure along the interface according to equations which include the effect of surface tension, fluid momentum, viscous effects and wettability. Neglecting gas momentum and motion of the gas inside the bubble would appear to be reasonable for a gas-liquid flow system, where the liquid density is 3 to 4 orders of magnitude higher than that of the gas. It also appears reasonable to assume a uniform pressure inside each bubble. By tracking the arbitrary shape which the gas-liquid interface can attain, the evolution of bubble shape can be realistically simulated.

In addition to solving the differential equations for the conservation of mass and momentum in the liquid phase, the position of the gas-liquid interface is defined by solving for the liquid volume fraction (f). This function equals one in a pure liquid region, and is zero in a pure gas region. Accordingly, f lies between 1 and 0 in any cell which contains a gas-liquid interface. From the mass conservation of the liquid phase, the time-dependent governing equation for f is

$$\frac{\partial f}{\partial t} + \frac{\partial (v_i f)}{\partial x_i} = 0 \tag{26}$$

The local curvature of the bubble surface, defined by the radius of curvature R, is related to the pressure difference across the gas-liquid boundary according to the Laplace-Young equation [35]

$$P_b - P = \frac{2\sigma}{R} \tag{27}$$

where P_b is the pressure in the bubble and P is the pressure of the liquid phase.

Pressure in the bubble is defined differently for growing and isolated bubbles. A growing bubble that is still attached to the gas injection hole has a gas source with a constant gas flow rate being injected. This bubble is assumed to be adiabatic, so the pressure inside the growing bubble (P_b) is related to its volume (V_b) by

$$V_b \frac{dP_b}{dt} + \gamma P_b \frac{dV_b}{dt} = \gamma P_g Q_g \tag{28}$$

where γ is the ratio of the specific heats of the gas, Q_g is the gas injection flow rate.

Bubbles that have detached from the injection hole are isolated from the gas source. In these bubbles, the pressure is related to volume by

$$P_b V_b^{\gamma} = constant \tag{29}$$

The standard, two-equation K-ε turbulence model is chosen to model turbulence, which requires the solution of two additional transport equations to find the turbulent kinetic energy, K, and the turbulent dissipation, ε, fields [36]. The liquid phase mass and momentum conservation equations, K-ε equations, and Equations 26-29 are discretized using the finite difference method and solved with the FLOW-3D v7.1 code developed by Flow Science, Inc. [37].

B. Preliminary results

A sequence of air bubble formation profiles is shown in Figure 17 for a numerical simulation of a typical experimental condition, with 2ml/s air flow rate injected horizontally from a 0.3mm hole into water flowing downward at 1m/s. The 3-D computational domain (5.3mm x 2mm x 4.6mm) simulates a small part of the liquid flow region near the gas injection hole for one symmetric half of the bubble.

The simulated bubble formation sequence qualitatively matches the experimental observations for this mode I case. The bubbles elongate slightly during the forming process. After disconnecting from the gas injection hole, the bubbles travel along the wall for a short distance before they detach from the wall and become spherical. Although this behavior matches the observations qualitatively, the quantitative match is not as good. The equivalent diameter of the simulated bubble (~ 0.6mm) is much smaller than the measurement (2.0mm) and the analytical model prediction (1.96mm). Many factors might contribute to this discrepancy, such as the boundary layer model (wall law), inlet conditions, bubble pressure assumptions, and numerical problems. Further work is needed to obtain more quantitative numerical simulations of bubble formation.

VII. ARGON BUBBLE SIZES IN LIQUID STEEL

Although the numerical model has difficulty producing a quantitative match with the water experiments, the analytical model is both accurate and fundamentally based. Thus, the analytical two-stage model was applied to estimate the initial size of argon bubbles expected in molten steel. Of particular interest is argon gas injection into slide-gate nozzles, which is used to avoid clogging in the nozzle which connects the tundish to the continuous casting mold.

A. Difference between steel-argon and water-air systems

In order to use a model validated for a water-air system to predict bubble size in a liquid steel-argon system, it is important to understand and account for the differences between the two systems. First, there are important differences in physical properties, despite the similar kinematic viscosities of molten steel and water. As listed in Table II,

the surface tension coefficient for steel-argon is more than 16 times of that of the water-air. The steel density is seven times that of water. Other important differences include the temperature and contact angles.

In the liquid steel-argon-ceramic system found in a steelmaking nozzle, the surface tension force might have more influence on bubble formation behavior due to the significant increase in surface tension, σ, and static contact angle, which is 150° [38]. Unfortunately, the advancing and receding contact angles needed in Equation 6 are unknown due to a lack of experimental data. The present air-water-plastic system observations suggest that the advancing contact angle θ_a should be larger than the static contact angle and increase with increasing liquid velocity. This restricts θ_O for the argon-steel-ceramic system to fall between 150 and 180°. Likewise, the receding contact angle θ_r should be smaller than θ_O and decrease with increasing liquid velocity. Putting these facts together suggests that the value of the contact angle function f_θ for the argon-steel-ceramic system might be close to that for the water-air-plastic system even though the three individual contact angles (θ_O, θ_a and θ_r) are very different between the two systems. For example, if θ_O, θ_a and θ_r had the plausible values of 150°, 155°, and 124° at U=0.9m/s, then f_θ for both systems would be 0.30. Thus, Equation 7 should provide reasonable estimates of f_θ for both systems.

Measurements [14] and calculations [34] both show that gas injected through the "hot" ceramic wall heats up to 99% of the liquid steel temperature even before it hits the liquid steel. Thus, the argon gas injection flow rate used in the model is the "hot" argon flow rate.

B. Analytical model predictions

The analytical model presented in Section IV is used to predict argon bubble sizes in liquid steel in a typical tundish nozzle with 78mm bore diameter for the range of conditions listed in Table II. Air bubble sizes in water are also predicted for the same conditions for comparison. The predictions are presented in Figures 18 and 19, which show the effects of gas injection flow rate and vertical liquid velocity on the predicted bubble diameters.

The argon bubble size increases with increasing gas flow rate and decreasing liquid velocity, with all of the same trends as observed in the air bubble – water system. Gas density is predicted to have no effect on argon bubble size in liquid steel for the same reason it is negligible in water-air systems. The small effect of the gas injection hole diameter is also similar in both systems.

For the same conditions, argon bubbles generated in liquid steel are predicted to be larger than air bubbles in water. The difference becomes more significant at lower liquid velocity and smaller gas flow rate. The reason for larger bubbles predicted in the steel-argon system is mainly due to the great difference in liquid density and surface tension coefficient. This increases both the drag force and the surface tension force acting during the expansion stage (I). The increase in the surface tension force is more than double the increase in the drag force, so the force balance of Equation 15 will be satisfied at a larger bubble size r_e, as compared with the water-air system. At very high liquid velocity, the drag force due to the flowing liquid becomes so dominant that the increase in surface tension becomes less important. Thus, the difference in bubble sizes between the two systems becomes smaller.

For the practical range of the liquid velocities found in tundish nozzles (0.7 - 1.2m/s), the difference in bubble size between the two systems is sometimes significant. For example, a typical tundish nozzle with 140 holes and 7 SLPM argon injection on UTN has 3.5 ml/s hot argon flow rate through each hole. At the mean liquid velocity of 0.7m/s, the argon bubbles diameters in liquid steel are about 1.5 times larger than the air bubble diameters in water. The corresponding argon bubble volumes are 3.4 times larger.

Figure 19 compares the predicted bubble sizes in steel and water as a function of liquid velocity for a few fixed gas flow rates. Much of the data is simply replotted from Figure 18. However, this figure illustrates more clearly how the bubble diameter increases greatly with decreasing liquid velocity. In fact, the two-stage model breaks down at very low liquid velocity conditions. The calculation [34] predicts infinite bubble sizes for U<0.5m/s for water-air system and U<0.7m/s for steel-argon system. This happens because the downward drag force at very low velocity is never able to balance the upward surface tension and buoyancy forces. Physically, the bubble might rise upwards in these cases. To properly predict the bubble size for this condition, the model would have to be modified to reverse the advancing and receding contact angle positions and include other forces important in stagnant flow from classic models.

C. Discussion

The elongation factor and contact angle function obtained from the water model experiments are used in the above liquid steel calculations due to the lack of better experimental data. The non-wetting property of the liquid metal on the ceramic wall encourages the forming bubble to spread more over the wall, relative to aqueous

systems.[12, 14, 19]. This might lead to a larger elongation factor, and consequently even larger argon bubbles than predicted here.

In a real nozzle with hundreds of pierced holes or thousands of tiny refractory pores, a continuous gas curtain might be expected on the gas injection section of the inner wall of the nozzle for Mode III. Moreover, the argon gas injected into the liquid steel has much bigger tendency to spread into a gas curtain on the refractory wall due to the much larger surface tension of the liquid steel and the non-wetting behavior of the liquid steel on the refractory material. This makes the bubble formation mode more likely to fall into Mode III at a lower liquid velocity than in the water-air system.

The water experiments showed that regardless of the bubble formation mode, the injected gas will always eventually detach from the wall, break up into discrete bubbles, and join into the liquid stream. Thus, there should be no gas curtain in a tundish nozzle beyond a short distance below the gas injection section. Instead, the argon bubbles in steel should have a greater tendency to have uneven size distributions after they detach from the wall and exit the nozzle with the steel. This detrimental situation can be avoided by reducing the argon flow rate through each hole or pore.

VIII. SUMMARY

The initial stages of bubble formation from one or two horizontal holes injecting gas into a shearing downward turbulent liquid flow are studied with water experiments and mathematical models. High-speed photography was used to quantify the contact angles, bubble elongation length, mode of bubble formation, bubble size, and size distribution for a wide range of conditions, approximating those in a tundish nozzle used

in continuous casting of steel. An analytical two-stage model is developed to predict the bubble size, with internal parameters taken solely from measurements. The predictions agree well with the measured sizes. A preliminary numerical simulation with a VOF model shows qualitative agreement with experimental observations of the bubble formation sequence, but more work is needed for a quantitative match. The analytical model is then used to predict the size of the argon bubbles generated in liquid steel of a tundish nozzle. The major findings of this work include:

- The mean bubble size increases with increasing gas injection flow rate.
- The mean bubble size increases with decreasing shearing liquid velocity.
- The mean bubble size in flowing liquid is significantly smaller than in stagnant liquid.
- The mean bubble size is relatively independent of gas injection hole size, especially at high liquid velocity
- The gas composition has little influence on bubble size.
- Bubble formation falls into one of four different modes, which depend primarily on the velocity of the flowing liquid and secondarily on the gas flow rate.
- In Mode I (low liquid speed and small gas flow rate), uniform-sized bubbles form and detach from the wall. In Mode III (high liquid speed), the injected gas elongates down along the wall and breaks into uneven sized bubbles. Mode II is intermediate between Mode I and Mode III. In Mode IV (high liquid speed and high gas flow rate), the gas elongates a long distance down the nozzle walls, forming a sheet before breaking up.

- It is possible to use Mode IV flow to prevent liquid contact with the wall, and thereby avoiding inclusion buildup and clogging. However, the gas injection rates are prohibitively high and other flow-related problems are likely.
- Compared to water-air system, argon bubbles in liquid steel should tend to spread more over the ceramic nozzle wall in liquid steel and fall into Mode II or III region. Thus, the argon bubbles likely have a larger tendency to have non-uniform sizes when detaching from the wall.
- Argon bubbles generated in liquid steel should be larger than air bubbles in water for the same flow conditions. The difference should become more significant at lower liquid velocity and smaller gas injection flow rate.

ACKNOWLEDGMENTS

The authors wish to thank the Continuous Casting Consortium at UIUC, including Allegheny Ludlum, (Brackenridge, PA), Armco Inc. (Middletown, OH), Columbus Stainless (South Africa), Inland Steel Corp. (East Chicago, IN), LTV Steel (Cleveland, OH), and Stollberg, Inc., (Niagara Falls, NY) for their continued support of our research. Final thanks are extended to Professor J. Muzumder (U. Michigan) for use of the high-speed video camera, and Flow Science, Inc. for FLOW-3D.

NOMENCLATURE

D	instantaneous equivalent bubble diameter (mm)
D_N	diameter of nozzle bore (mm)
d	gas injection hole diameter (mm)

$_d$	subscript referring to instant of detachment, stage 2
e	elongation factor (=L/D)
$_e$	subscript referring to end of expansion, stage 1
F_B	buoyancy force for a bubble (N)
F_D	drag force acting on bubble from flowing liquid (N)
F_S	surface tension force on bubble (N)
F_{Sz}	vertical component of surface tension force on bubble (N)
f	frequency of bubble formation (s^{-1})
f_θ	contact angle function, $f_\theta = sin\theta_O(cos\theta_r - cos\theta_a)$
L	elongation length at instant of detachment ($=e_d D_b$) (mm)
Q_g	gas injection flow rate per hole (ml/s)
r	horizontal radius of an ellipsoidal bubble (mm)
Re_{bub}	Reynolds number of bubble ($=uD/\upsilon$)
t	time during bubble formation (s)
U	average liquid velocity in nozzle (m/s)
u	liquid velocity profile across nozzle bore =u(y) (m/s)
$\bar{u}$	average liquid velocity across bubble (m/s)
V	bubble volume ($=\pi D^3/6$) (ml)
y, z	horizontal and vertical coordinate directions (m)
μ_g , μ_l	molecular viscosity of gas and liquid (kg/m-s)
θ_o	static contact angle (°)
θ_a , θ_r	advancing and receding contact angles of a forming bubble (°)
ρ_g , ρ_l	density of gas and liquid (kg/m^3)

σ liquid surface tension (N/m)

υ kinematic viscosity of liquid $=(\mu_l/\rho_l)$ (m^2/s)

REFERENCES

1. N. Bessho, R. Yoda, T. Yamasaki, T. FUji and T. Nozaki: "Numerical Analysis of Fluid Flow in the Continuous Casting Mold by a Bubble Dispersion Model", *Transactions of the ISS (I$SM),* 1991, (April), pp. 39-44.

2. B.G. Thomas and X. Huang: "Effect of Argon Gas on Fluid Flow in a Continuous Slab Casting Mold", *76th Steelmaking Conference*, Dallas, TX, Iron and Steel Society, 1993, vol. 76, pp. 273-289.

3. B.G. Thomas, X. Huang and R.C. Sussman: "Simulation of Argon Gas Flow Effects in a Continuous Slab Caster", *Metallurgical Transactions B,* 1994, vol. 25B (4), pp. 527-547.

4. B.G. Thomas, A. Dennisov and H. Bai: "Behavior of Argon Bubbles during Continuous Casting of Steel", *80th ISS Steelmaking Conference*, Chicago, 1997, pp. 375-384.

5. J. Knoepke and M. Hubbard: "Pencil Blister Reductions at Inland Steel Company", *77th Steelmaking Conference*, Washington, D. C, 1994, pp. 381-388.

6. L. Wang, H.-G. Lee and P. Hayes: "Prediction of the Optimum Bubble Size for Inclusion Removal from Molten Steel by Flotation", *ISIJ International,* 1996, vol. 36 (1), pp. 7-16.

7. K. Tabata, T. Kakehi and M. Terao: *Gas Injection Methods at Tundish Slide Gate Valve for Continuous Casting*, Shinagawa Technical Report, Report No. 31, 1988.

8. M. Sano and K. Mori: "Bubble Formation from Single Nozzles in Liquid Metals", *Trans. JIM,* 1976, vol. 17, pp. 344-352.

9. A. Thomas, S. Tu and D. Janke: "Frequency of Bubble Formation in Water and Liquid Iron", *Steel Research,* 1997, vol. 68 (5), pp. 198-200.

10. M. Sano, Y. Fujita and K. Mori: "Formation of Bubbles at Single Nonwetted Nozzles in Mercury", *Metallurgical Transactions B,* 1976, vol. 7B (June), pp. 300-301.

11. M. Iguchi, H. Kawabata, K. Nakajima and Z. Morita: *Metallurgical Transactions B,* 1995, vol. 26B, pp. 67.

12. G.A. Irons and R.I.L. Guthrie: "Bubble Formation at Nozzles in Pig Iron", *Metallurgical Transactions B,* 1978, vol. 9B (March), pp. 101-110.

13. K.G. Davis, G.A. Irons and R.I.L. Guthrie: "X-Ray Cinematographic Observations of Gas Injection into Liquid Metals", *Metallurgical Transactions B,* 1978, vol. 9B (December), pp. 721-722.

14. M. Iguchi, T. Chihara, N. Takanashi, Y. Ogawa, N. Tokumitsu and Z. Morita: "X-ray Fluoroscopic Observation of Bubble Characteristics in a Molten Iron Bath", *ISIJ International,* 1995, vol. 35 (11), pp. 1354-1361.

15. R. Kumar and N.R. Kuloor: "The Formation of Bubbles and Drops", in *Advances in Chemical Engineering*, vol. 8, Academic Press, New York, London, 1970, pp. 255-368.

16. R. Clift, J.R. Grace and M.E. Weber: *Bubbles, Drops, and Particles*, Academic Press Inc., 1978.

17. H. Tsuge: "Hydrodynamics of Bubble Formation from Submerged Orifices", in *Encyclopedia of Fluid Mechanics*, vol. 3, Gulf Publishing Co., Houston, TX, 1986, pp. 191-232.

18. N. Rabiger and A. Vogelpohl: "Bubble Formation and its Movement in Newtonian and Non-Newtonian Liquid", in *Encyclopedia of Fluid Mechanics*, vol. 3, Gulf Publishing Co., Houston, TX, 1986, pp. 58-88.

19. Z. Wang, K. Mukai and D. Izu: "Influence of Wettability on the Behavior of Argon Bubbles and Fluid Flow inside the Nozzle and Mold", *ISIJ International,* 1999, vol. 39 (2), pp. 154-163.

20. J.F. Davidson and B.O.G. Schuler: "Bubble Formation at an Orifice in an Inviscid Liquid", *Trans. Instn Chem. Engrs,* 1960, vol. 38, pp. 335-342.

21. R. Kumar and N.R. Kuloor: *Chem. Tech.,* 1967, vol. 19, pp. 733.

22. W.V. Pinczewski: "The Formation and Growth of Bubbles at a Submerged Orifice", *Chemical Engineering Science,* 1981, vol. 36, pp. 405-411.

23. K. Terasaka and H. Tsuge: "Bubble Formation at a Single Orifice in Highly Viscous Liquids", *Journal of Chemical Engineering of Japan,* 1990, vol. 23 (2), pp. 160-165.

24. K. Terasaka and H. Tsuge: "Bubble Formation under Constant-Flow Conditions", *Chemical Engineering Science,* 1993, vol. 48 (19), pp. 3417-3422.

25. H. Tsuge, Y. Nakajima and K. Terasaka: "Behavior of Bubble Formed from a Submerged Orifice under High System Pressure", *Chemical Engineering Science,* 1992, vol. 47 (13/14), pp. 3273-3280.

26. T. Hong, C. Zhu and L.-S. Fan: "Numerical Modeling of Formation of Single Bubble Chain and Bubble Breakage due to Collision with Particle in Liquid", *1996 ASME Fluids Division Conference*, 1996, vol. FED 236, pp. 581-588.

27. C.W. Hirt and B.D. Nichols: "Volume of Fluid (VOF) Method for the Dynamics of Free Boundary", *Journal of Computational Physics,* 1981, vol. 39, pp. 201-225.

28. S.C. Chuang and V.W. Goldschmidt: "Bubble Formation due to a Submerged Capillary Tube in Quiescent and Coflowing Streams", *Journal of Basic Engineering,* 1970, vol. 92, pp. 705-711.

29. Y. Kawase and J.J. Ulbrecht: "Formation of Drops and Bubbles in Flowing Liquids", *Ind. Eng. Chem. Process Des. Dev.,* 1981, vol. 20 (4), pp. 636-640.

30. I.B.V. Morgenstern and A. Mersmann: "Aeration of Highly Viscous Liquids", *Germany Chemical Engineering,* 1982, vol. 5, pp. 374-379.

31. M. Burty, M. Larrecq, C. Pusse and Y. Zbaczyniak: "Experimental and Theoretical Analysis of Gas and Metal Flows in Submerged Entry Nozzles in Continuous Casting", *13th PTD Conference*, Nashville, TN, 1995, vol. 13, pp. 287-292.

32. R.H.S. Winterton: "Sizes of Bubbles Produced by Dissolved Gas Coming out of Solution on the Walls of Pipes in Flowing Systems", *Chemical Engineering Science,* 1972, vol. 27, pp. 1223-1230.

33. R.H.F. Pao: *Fluid Dynamics*, Merrill, 1967.

34. H. Bai: *Argon Bubble Behavior in Slide-Gate Nozzles during Continuous Casting of Steel Slabs*, Ph.D. Thesis, University of Illinois at Urbana-Champaign, 2000.

35. S.L. Soo: *Multiphase Fluid Dynamics*, Science Press, Gower, 1990.

36. B.E. Launder and D.B. Spalding: "Numerical Computation of Turbulent Flows", *Comp. Meth. Applied Mechanics and Engr.,* 1974, vol. 13, pp. 269-289.

37. Flow Science Inc.: *FLOW-3D User's Manual*, 1997.

38. L. Jimbo, A. Sharan and A.W. Cramb: "Recent measurements of surface and interfacial tensions in steels", *76th SteelMaking Conference*, Dallas, TX, 1993, pp. 485-494.

FIGURE AND TABLE CAPTIONS

Table I Average contact angles measured in the water experiments

Table II Physical properties and operating conditions used in the two-stage model

Figure 1 Schematic of water experiment for bubble formation study

Figure 2 Measured air bubble sizes in stagnant water compared with Iguchi's empirical correlation

Figure 3 Effect of gas injection rate and water velocity on modes and measured bubble sizes (mean equivalent sphere diameter) and size range (a) 0.2mm injection hole diameter (b) 0.3mm injection hole diameter (c) 0.4mm injection hole diameter

Figure 4 Mean air bubble volumes measured in stagnant and flowing water

Figure 5 Effect of gas composition, gas flow rate and liquid velocity on measured bubble size

Figure 6 Figure 6 Example experiment photographs and schematics showing the four different bubble formation modes (a) Mode I, side view (b) Mode II, side view (c) Mode III, side view (d) Mode IV, side view (e) Mode I, end view (f) traced schematic of Mode I, end view (g) traced schematic of Mode III, end view (h) Mode III, end view (i) Mode IV, end view

Figure 7 Photograph series showing the bubble formation process for Mode I and Mode III (a) Mode I -U=0.9m/s, Q_G=0.5ml/s, d=0.4mm, Bubble frequency f=293/s, Equivalent bubble diameter: measured: 1.51mm, predicted: 1.53mm (b) Mode III - U=1.9m/s, Q_G=1.86ml/s, d=0.3mm, Bubble frequency f=444/s, Equivalent bubble diameter: measured: 2.0mm, predicted:1.95mm

Figure 8 Bubble formation sequence traced from Figure 7 (a) Mode I (b) Mode III

Figure 9 Bubble elongation length measured at instant of bubble detachment from the gas injection hole (a) Schematic of the measurement (b) Measured elongation (*L*)

Figure 10 Measured and fitted elongation factors at bubble detachment (a) effect of gas injection (b) effect of liquid velocity

Figure 11 Schematic bubble shapes showing advancing and receding contact angles (a) water-air system - measured (b) steel-argon system - expected

Figure 12 Effect of mean liquid velocity on measured and fitted contact angle function

Figure 13 Schematic of liquid velocity profile near wall region and forces acting on a growing bubble

Figure 14 Evolution of estimated vertical forces acting on a bubble growing in water

Figure 15 Idealized sequence of bubble formation in the two stage model (a) expansion stage (b) elongation stage

Figure 16 Comparison of measured and predicted air bubble sizes in water for different gas flow rates, liquid velocities, and injection hole sizes (a) U=0.9m/s (b) U=1.4m/s (c) U=1.9m/s (d) U=2.5m/s

Figure 17 Simulated bubble formation sequence calculated using VOF model

Figure 18 Comparison of the predicted argon bubble size in liquid steel with air bubble size in water

Figure 19 Effect of liquid velocity and gas flow rate on size of argon bubbles in liquid steel and air bubbles in water

Table I Average contact angles measured in the water experiments

Average liquid velocity U (m/s)	Static contact angle θ_O (°)	Advancing contact angle θ_a (°)	Receding contact angle θ_r (°)	Contact angle function $f_\theta = \sin\theta_O(\cos\theta_r-\cos\theta_a)$
0.9	50	64	35	0.30
1.4	50	82	29	0.56
1.9	50	101	22	0.85
2.5	50	134	27	1.26

Table II Physical properties and operating conditions used in the two-stage model

Parameters	Symbol	Unit	Water-air system	Steel-hot argon system
Liquid density	ρ_l	Kg/m^3	1000	7021
Gas density	ρ_g	Kg/m^3	1.29	0.27
Liquid viscosity	μ_l	kg/(ms)	0.001	0.0056
Gas viscosity	μ_g	kg/(ms)	1.7E-5	7.42E-5
Surface tension coefficient	σ	N/m	0.073	1.192
Gas injection flow rate per pore	Q_g	ml/s	0.1 - 6 ml/s	0.1 - 6 ml/s
Nozzle diameter	D_n	mm	35	78
Diameter of gas injection hole	d	mm	0.2, 0.3, 0.4	0.2, 0.3, 0.4
Average velocity 0of the liquid	U	m/s	0.9, 1.4, 1.9, 2.5	0.7, 0.9, 1.4,1.9, 2.5
Elongation factor at detachment	e_d		1.32, 1.53,1.67, 1.76	Equation 7
Contact angle function $f_\theta=\sin\theta_o(\cos\theta_r-\cos\theta_a)$	f_θ		0.30, 0.56, 0.85, 1.26	Equation 4

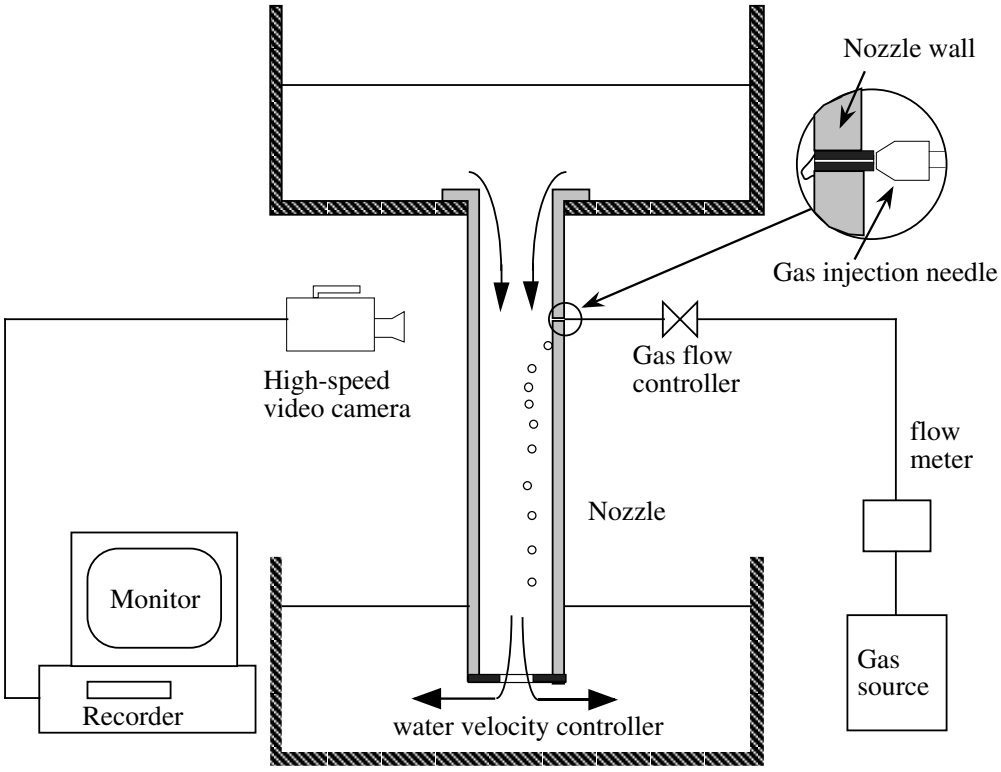

Figure 1 Schematic of water experiment for bubble formation study

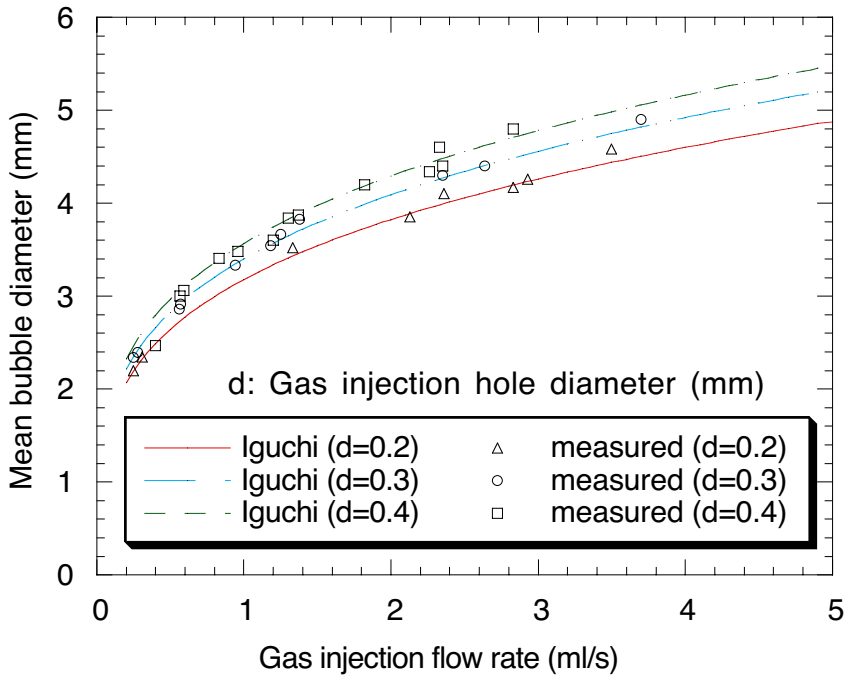

Figure 2 Measured air bubble sizes in stagnant water compared with Iguchi's empirical correlation [34]

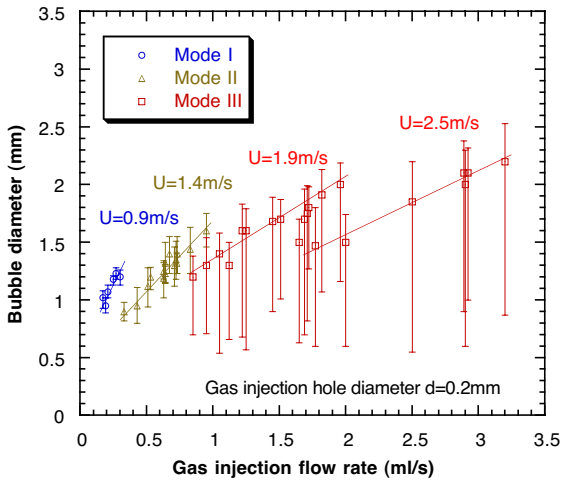

(a)

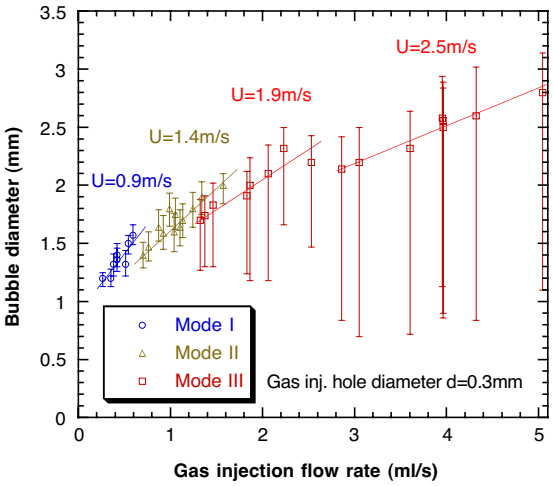

(b)

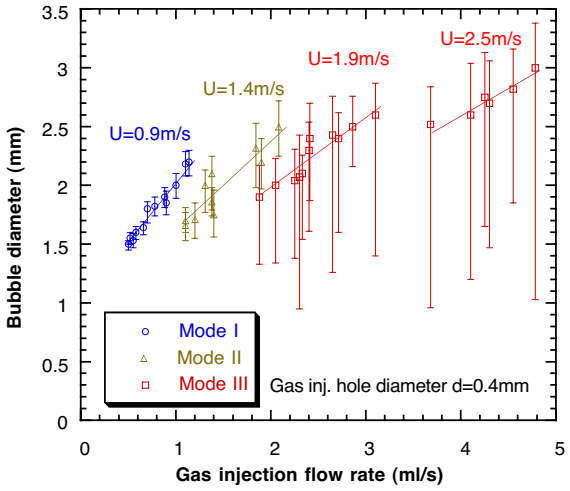

(c)

Figure 3 Effect of gas injection rate and water velocity on modes and measured bubble sizes (mean equivalent sphere diameter) and size range (a) 0.2mm injection hole diameter (b) 0.3mm injection hole diameter (c) 0.4mm injection hole diameter

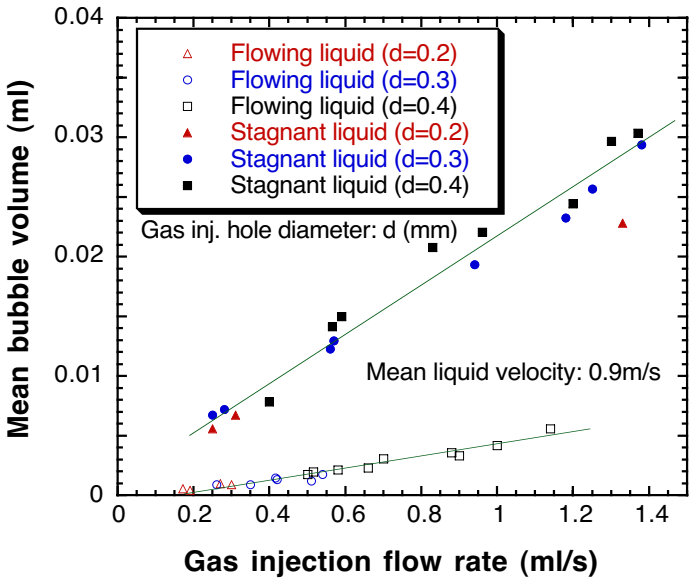

Figure 4 Mean air bubble volumes measured in stagnant and flowing water

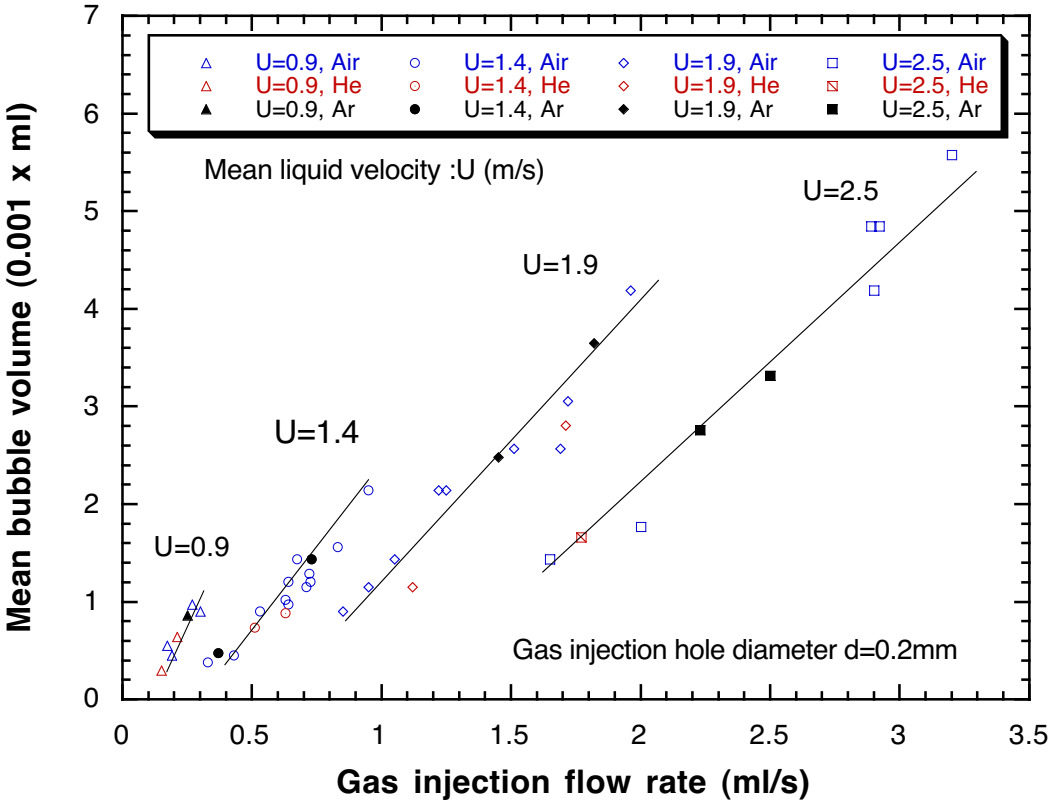

Figure 5 Effect of gas composition, gas flow rate and liquid velocity on measured bubble size

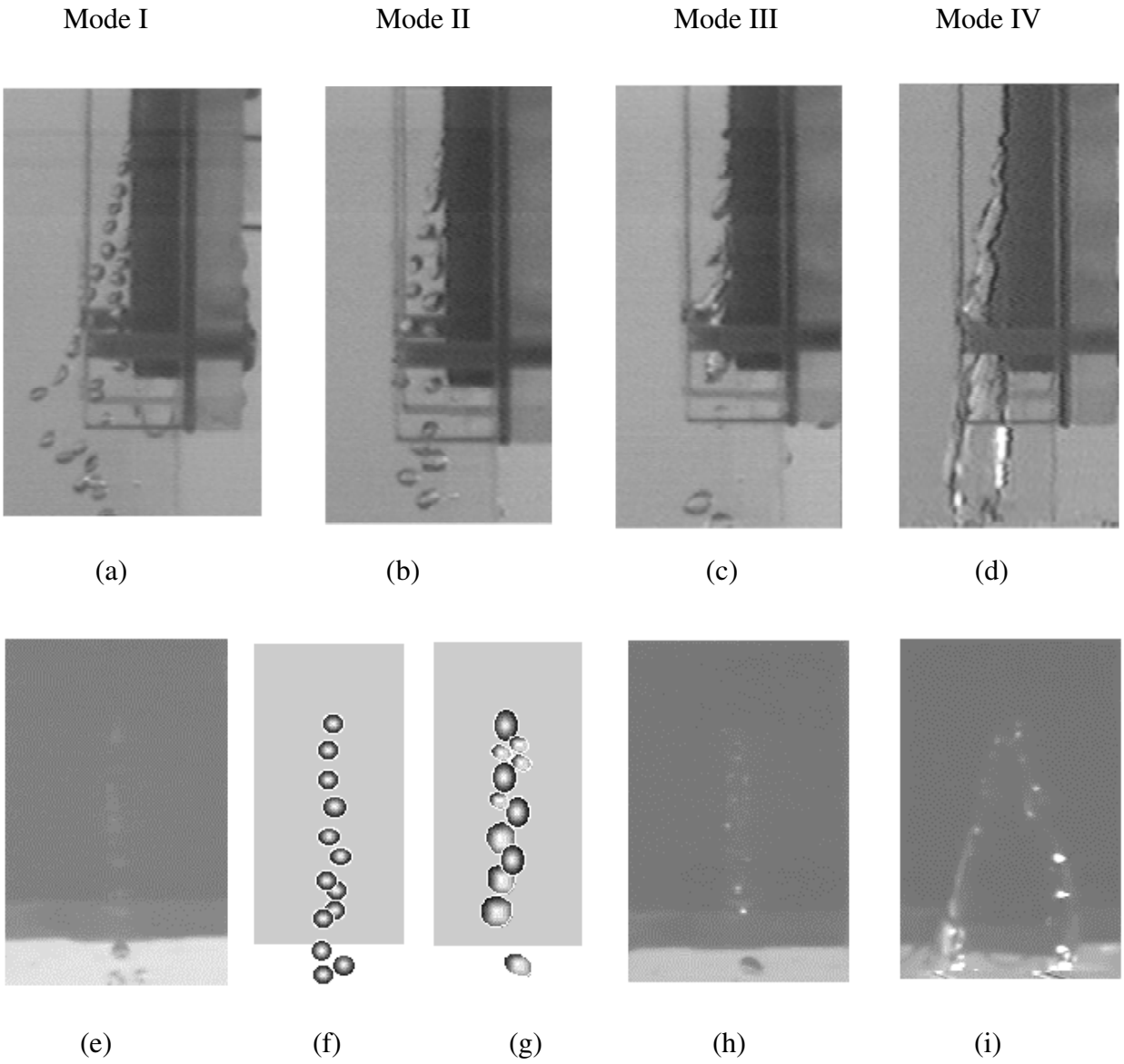

Figure 6 Example experiment photographs and schematics showing the four different bubble formation modes (a) Mode I, side view (b) Mode II, side view (c) Mode III, side view (d) Mode IV, side view (e) Mode I, end view (f) traced schematic of Mode I, end view (g) traced schematic of Mode III, end view (h) Mode III, end view (i) Mode IV, end view

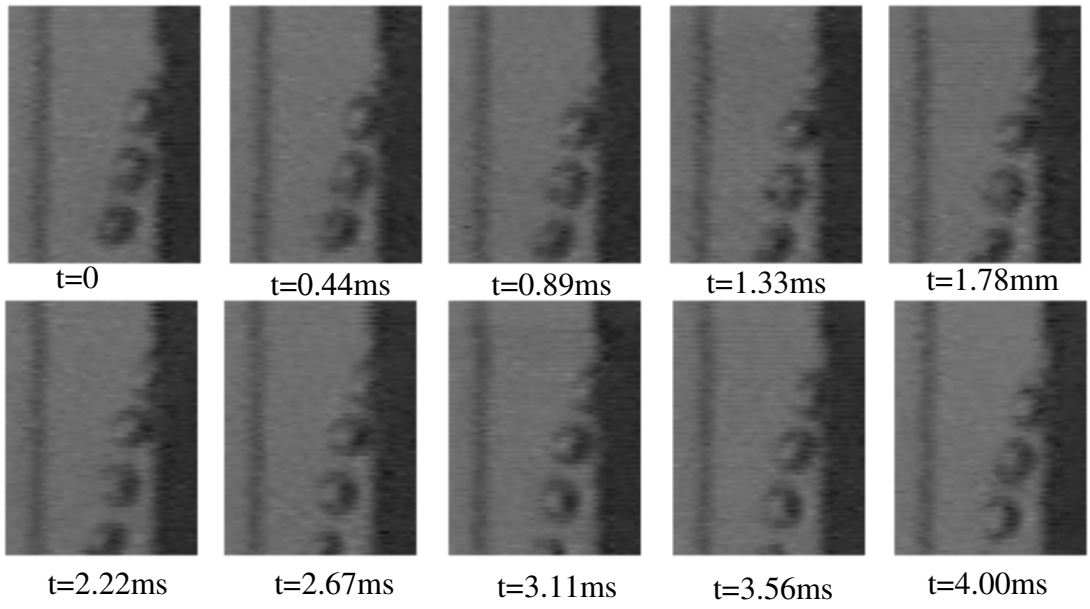

(a)

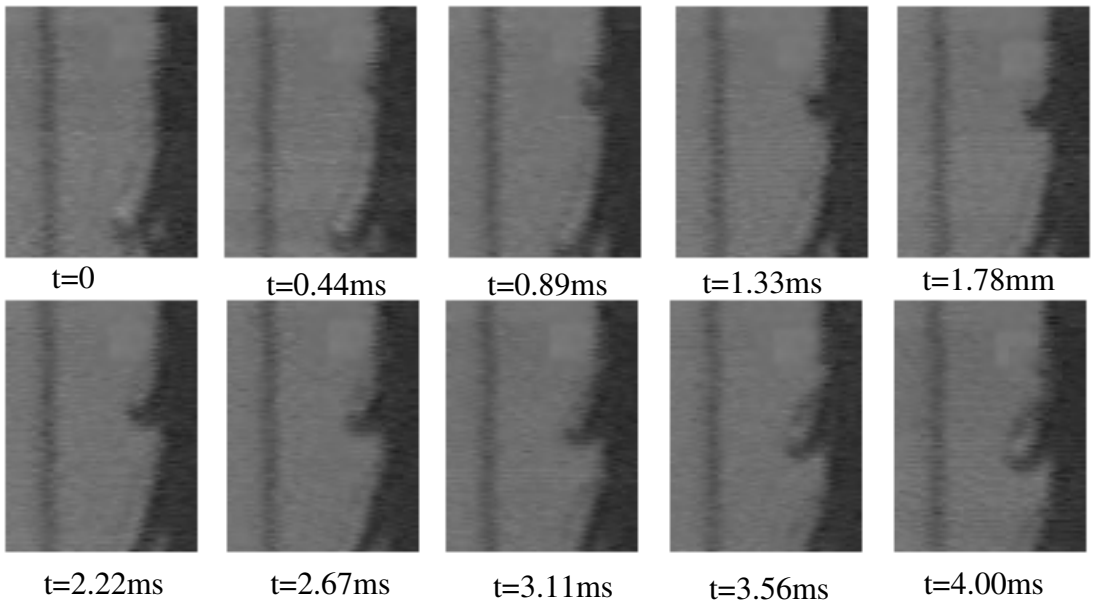

(b)

Figure 7 Photograph series showing the bubble formation process for Mode I and Mode III
(a) Mode I -- U=0.9m/s, Q_G=0.5ml/s, d=0.4mm, Bubble frequency f=293/s,
Equivalent bubble diameter: measured: 1.51mm, predicted: 1.53mm
(b) Mode III --U=1.9m/s, Q_G=1.86ml/s, d=0.3mm, Bubble frequency f=444/s,
Equivalent bubble diameter: measured: 2.0mm, predicted:1.95mm

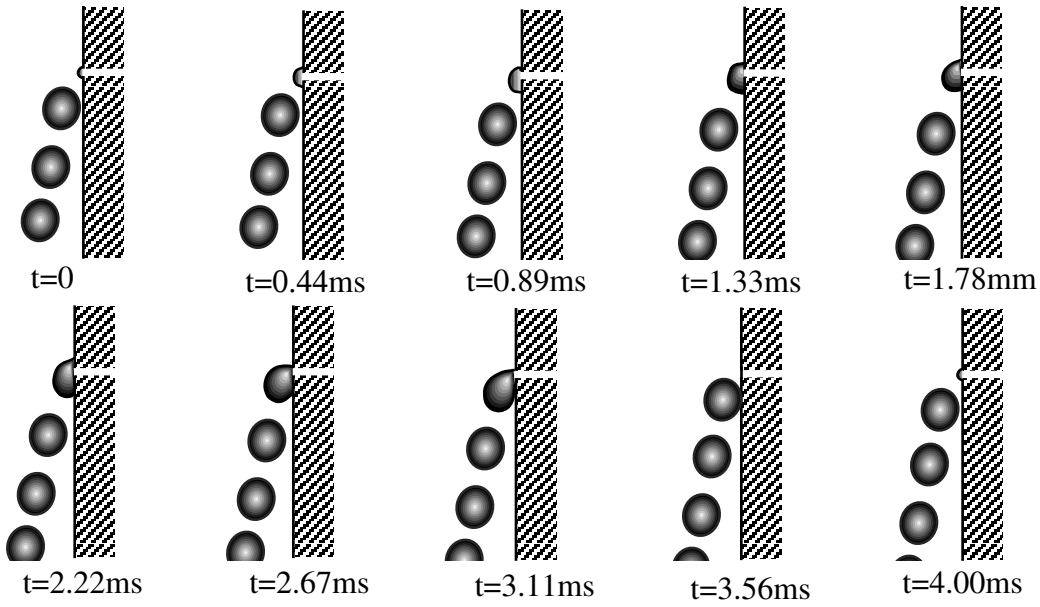

(a)

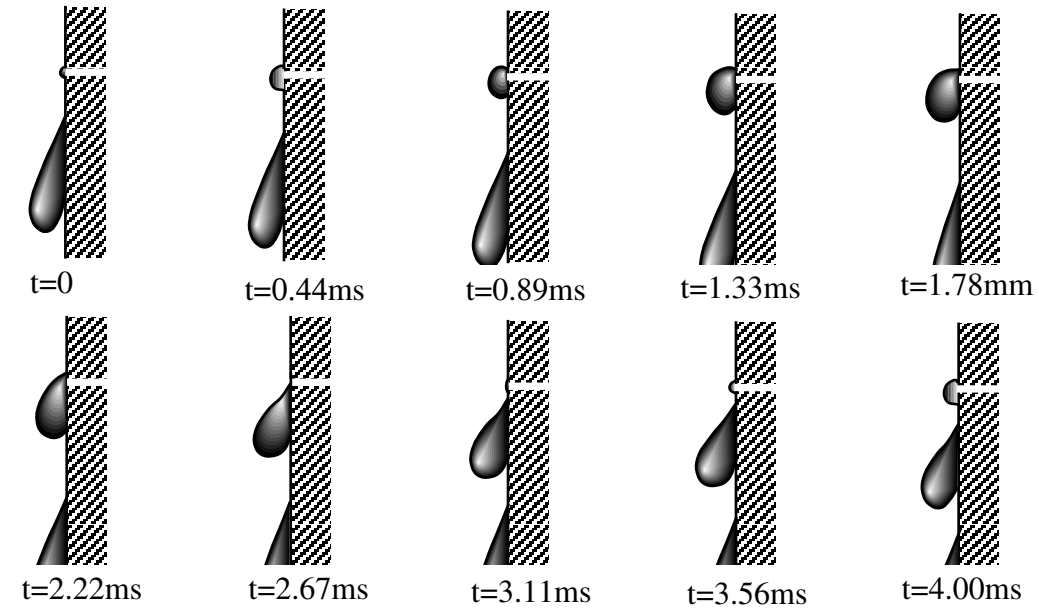

(b)

Figure 8 Bubble formation sequence traced from Figure 7 (a) Mode I (b) Mode III

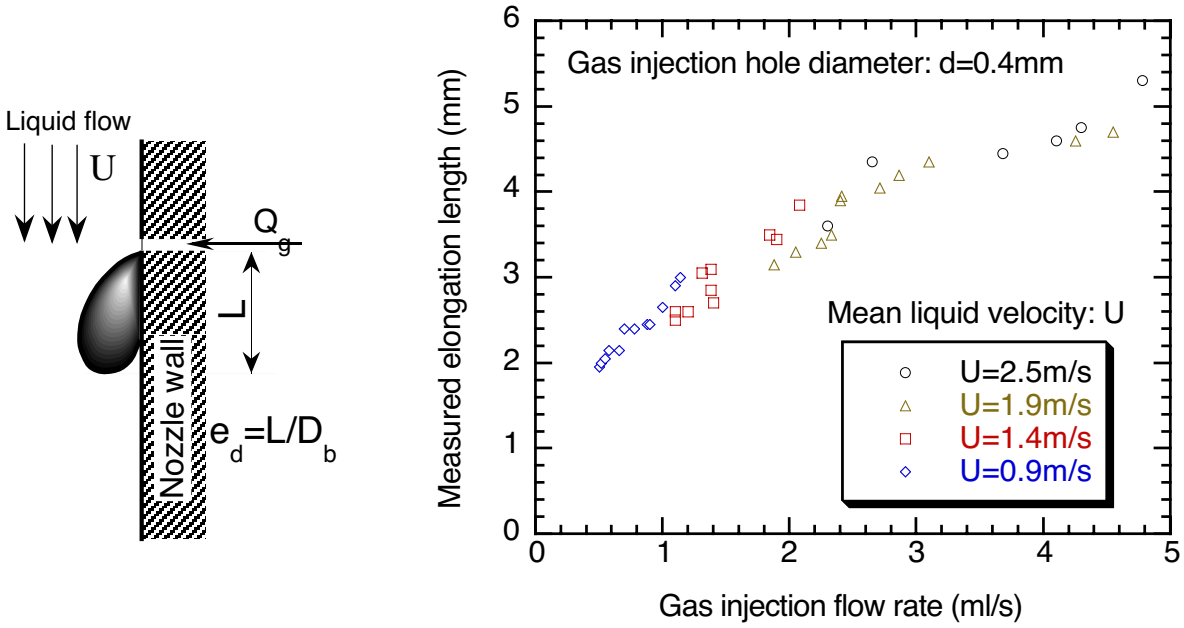

(a) (b)

Figure 9 Bubble elongation length measured at instant of bubble detachment from the gas injection hole (a) Schematic of the measurement (b) Measured elongation (L)

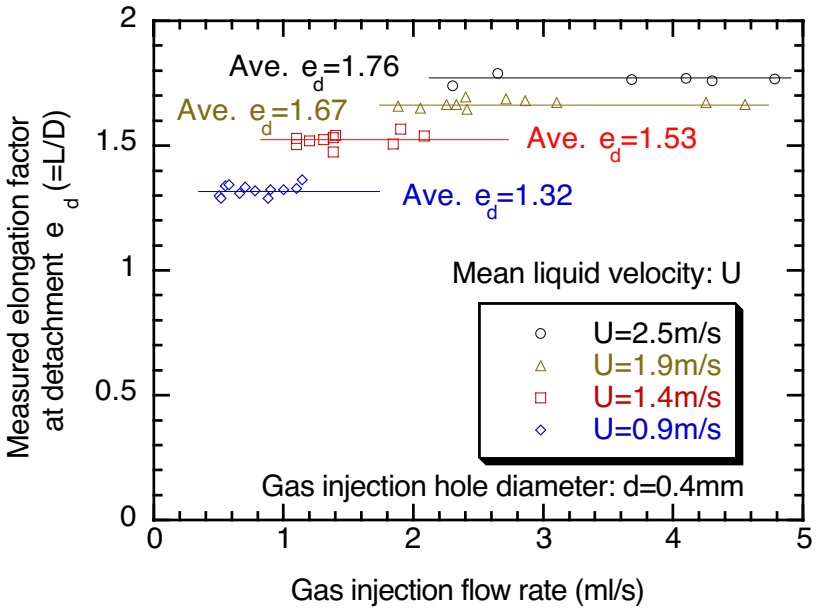

(a)

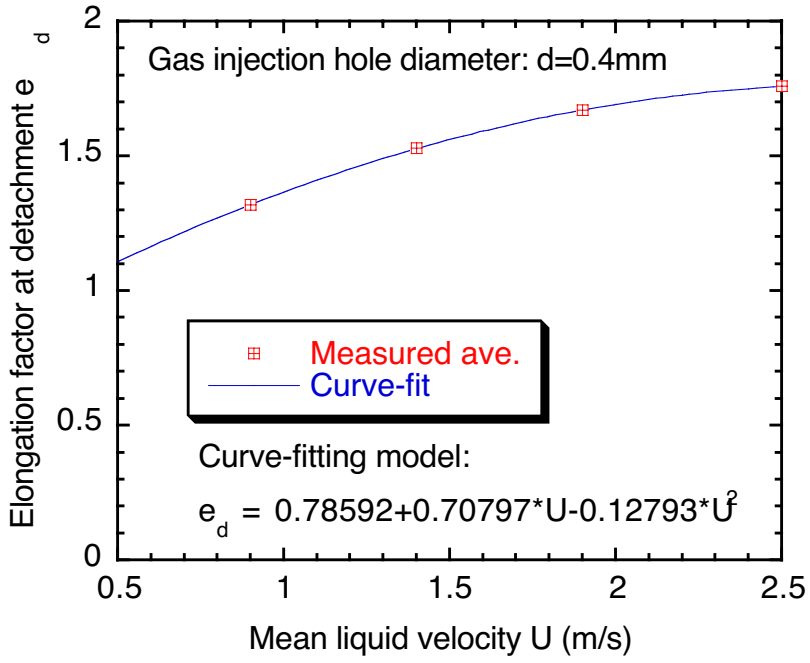

(b)

Figure 10 Measured and fitted elongation factors at bubble detachment (a) effect of gas injection (b) effect of liquid velocity

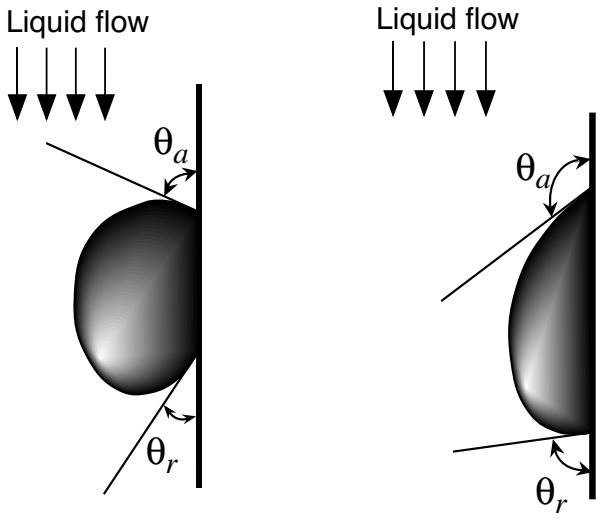

(a) (b)

Figure 11 Schematic bubble shapes showing advancing and receding contact angles (a) water-air system - measured (b) steel-argon system - expected

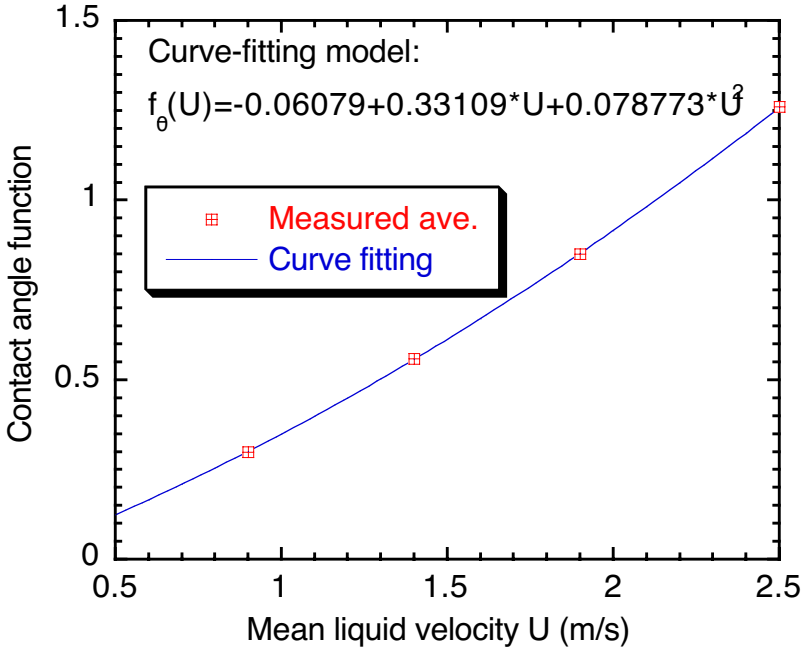

Figure 12 Effect of mean liquid velocity on measured and fitted contact angle function

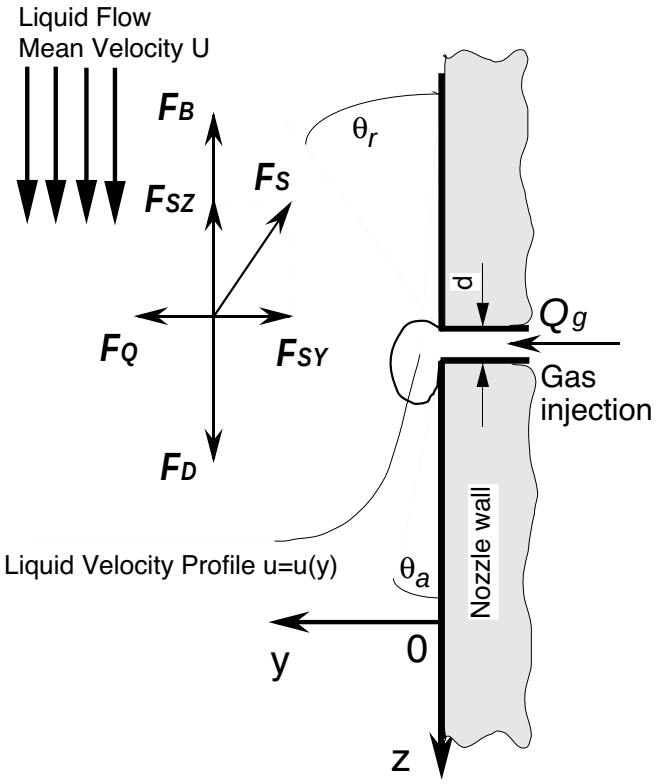

Figure 13 Schematic of liquid velocity profile near wall region and forces acting on a growing bubble

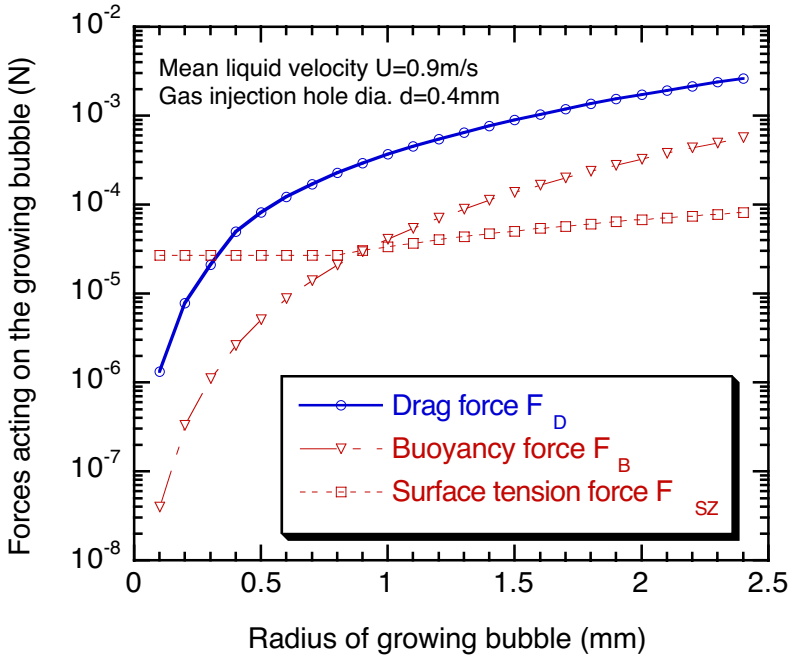

Figure 14 Evolution of estimated vertical forces acting on a bubble growing in water

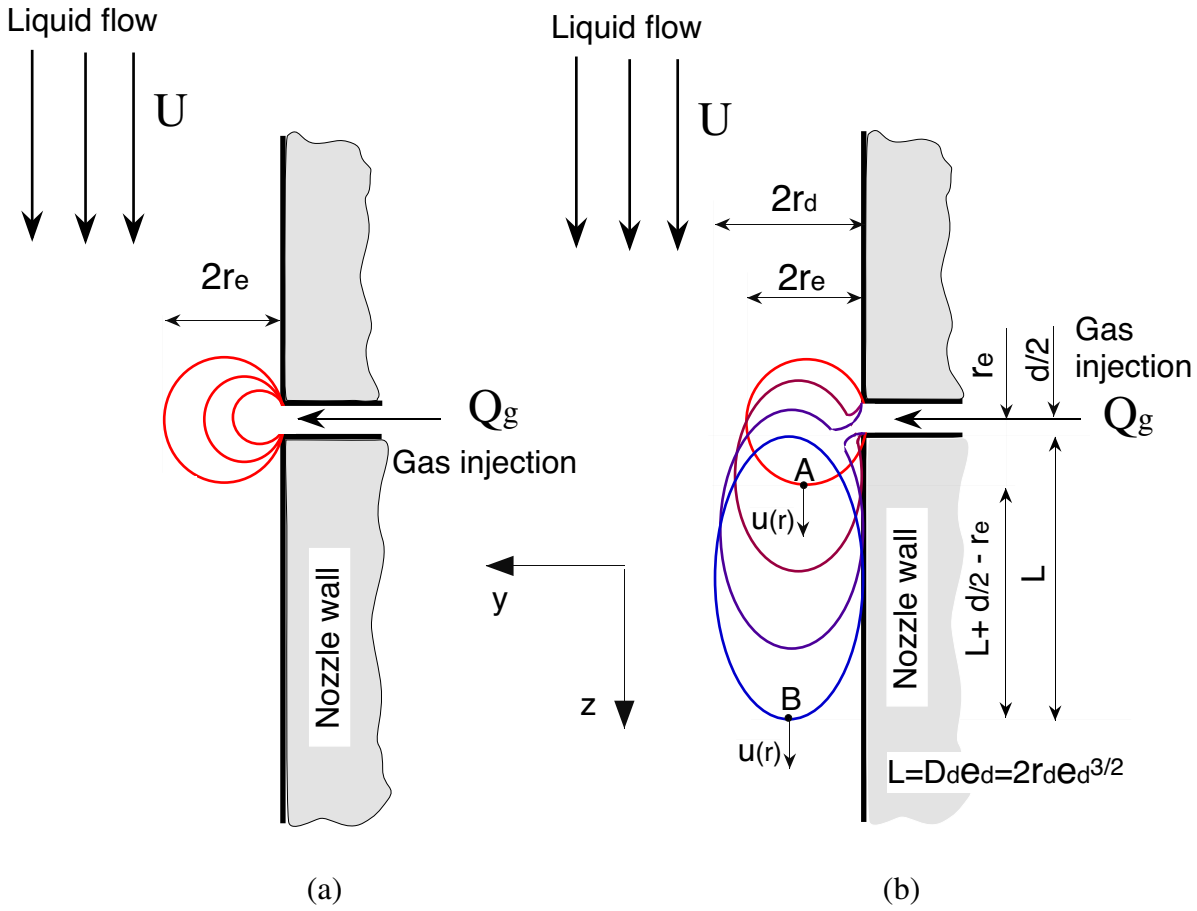

Figure 15 Idealized sequence of bubble formation in the two stage model
(a) expansion stage (b) elongation stage

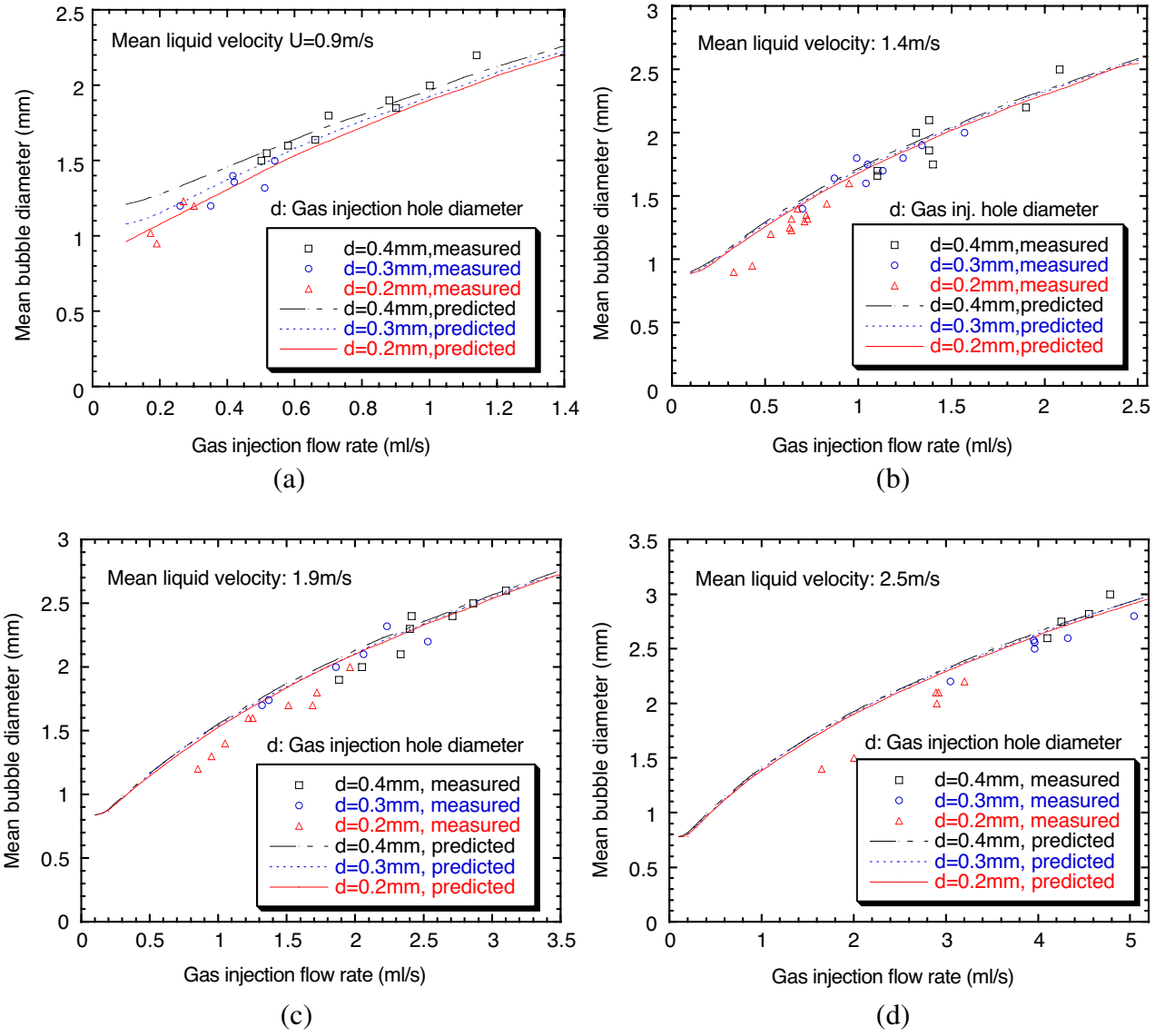

Figure 16 Comparison of measured and predicted air bubble sizes in water for different gas flow rates, liquid velocities, and injection hole sizes
(a) U=0.9m/s (b) U=1.4m/s (c) U=1.9m/s (d) U=2.5m/s

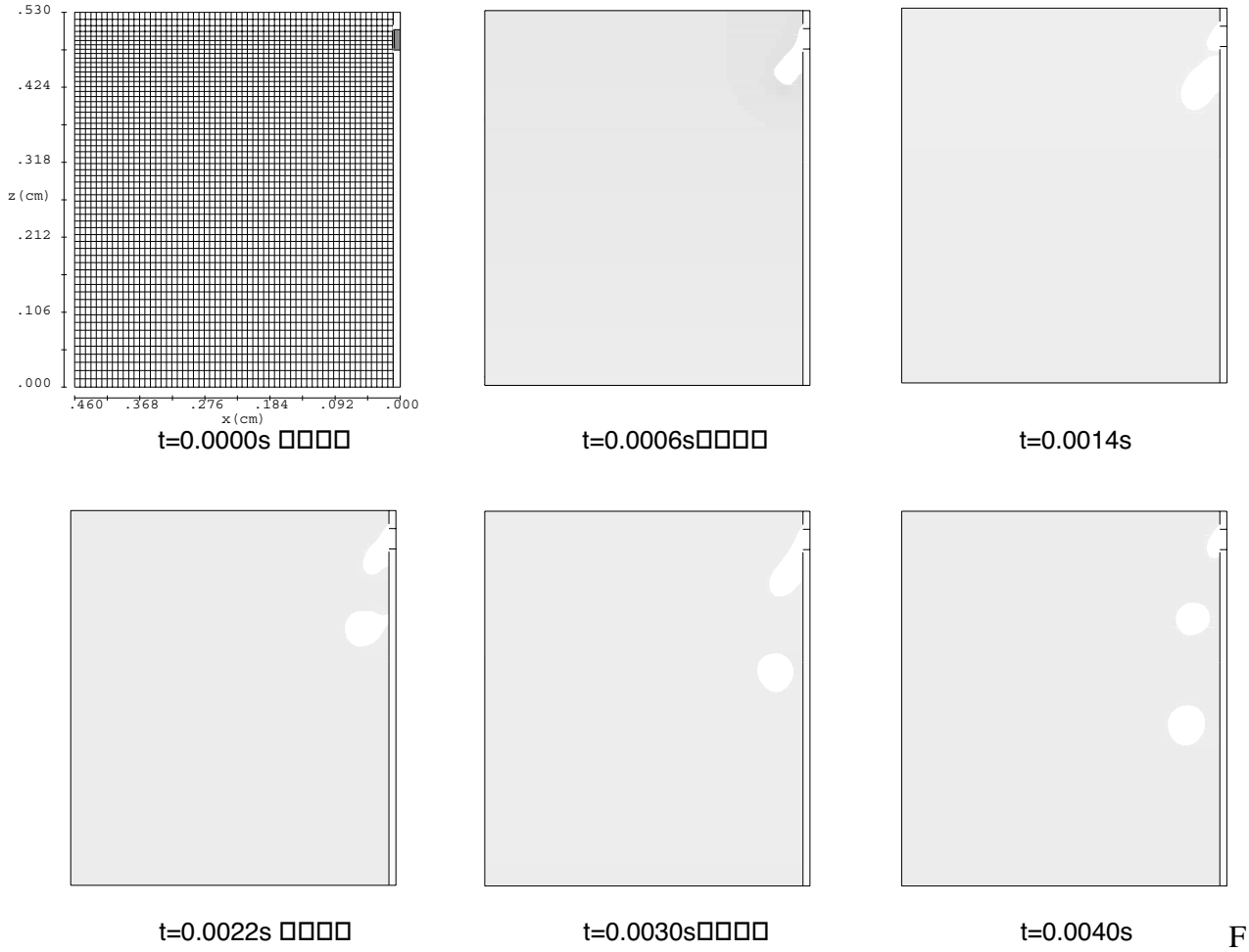

Figure 17 Simulated bubble formation sequence calculated using VOF model

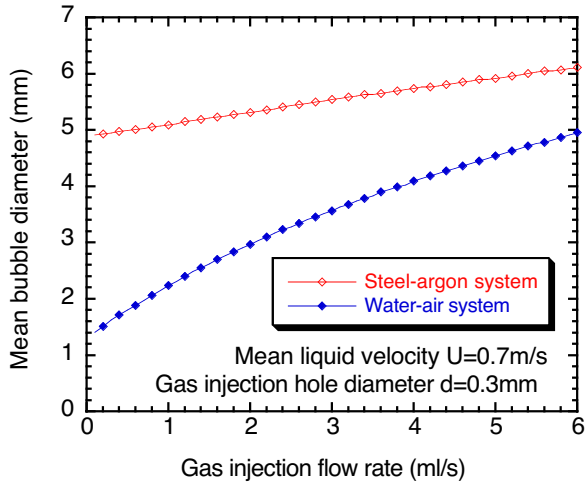

(a)

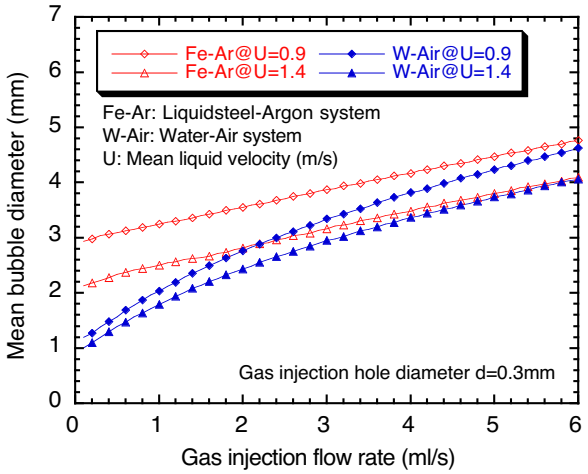

(b)

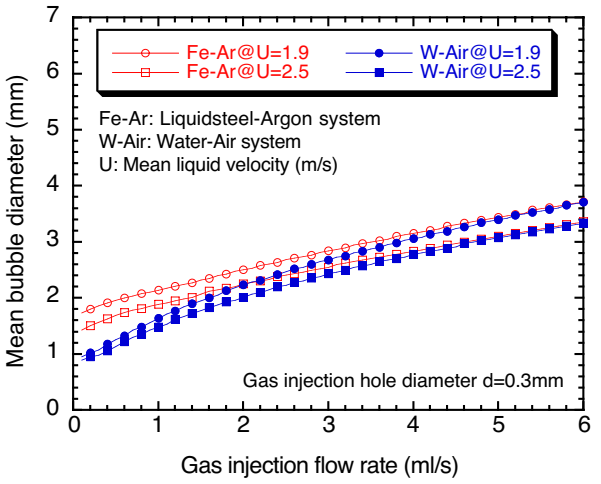

(c)

Figure 18 Comparison of the predicted argon bubble size in liquid steel with air bubble size in water

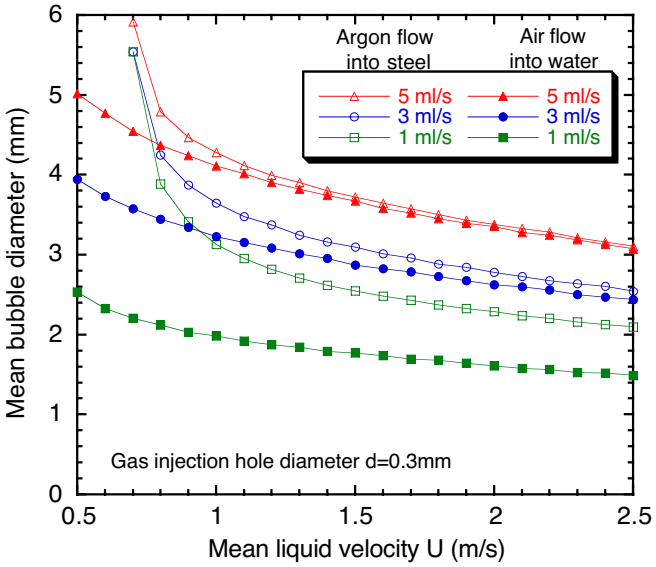

Figure 19 Effect of liquid velocity and gas flow rate on size of argon bubbles in liquid steel and air bubbles in water